①

AD-A202 706

DEPARTMENT OF THE AIR FORCE

AIR UNIVERSITY

AIR FORCE INSTITUTE OF TECHNOLOGY

Wright-Patterson Air Force Base, Ohio

89   1 17 005

AFIT/GAE/AA/88D-10

DEVELOPMENT OF A SHOCK CAPTURING
CODE FOR USE AS A TOOL IN DESIGNING
HIGH-WORK LOW ASPECT RATIO TURBINES

THESIS

Mark A. Driver
Captain, USAF

AFIT/GAE/AA/88D-10

DTIC
SELECTED
JAN 1 8 1989
H

Approved for public e release; distribution unlimited

AFIT/GAE/AA/88D-10

DEVELOPMENT OF A SHOCK CAPTURING CODE FOR USE AS A TOOL IN

DESIGNING HIGH-WORK LOW ASPECT RATIO TURBINES

THESIS

Presented to the Faculty of the School of Engineering

of the Air Force Institute of Technology

Air University

In Partial Fulfillment of the

Requirements for the Degree of

Master of Science in Aeronautical Engineering

Mark A. Driver, B.A.E.

Captain, USAF

December 1988

Preface

The main objective of this effort is to develop a code that yields a reasonably accurate loading diagram for a typical high-work gas turbine. A practical execution time to enable a designer to quickly arrive at an acceptable blade shape is a secondary objective.

Two people deserve special mention for their assistance and encouragement. I am particularly indebted to Lt Col Jack Mattingly of the Aero-Propulsion Laboratory for sharing his enthusiasm and knowledge. It was a joy and a privilege to be his student. The success of this project is largely due to Mr. Robert Gray, the project sponsor, also of the Aero-Propulsion Laboratory. Bob's love of engineering, fascination with the basic physics, and mastery of mathematics made this effort both enjoyable and achievable.

I wish to thank my thesis advisor, Dr. Ahmed Halim, for his assistance throughout the effort. Thanks also to Dr. Joseph Shang and Lt David Amdahl of the Flight Dynamics Laboratory. Dr. Shang was willing to share his expertise and provide assistance whenever called upon. Lt Amdahl graciously provided the grid generation code along with instructions for its use. Finally, the greatest debt is owed to my wife ████ for her patience and understanding through the many days and nights I spent in front of a computer terminal.

<div align="right">

Mark A. Driver

</div>

Table of Contents

For
ɛI   ☑
·d   ☐
.ion   ☐

By
Distribution/
Availability Codes
Avail and/or
Dist   Special

A-1

List of Figures

List of Tables

List of Symbols

A	characteristic location
a	speed of sound
B	characteristic location
C	characteristic location; chord length
C_p	specific heat at constant pressure
CFL	Courant-Friedrich-Lewy condition
cm	distance in centimeters
E	vector of dependent variables
E_t	total energy per unit volume
e	internal energy
F	vector of dependent variables
H	total or stagnation enthalpy
h	static enthalpy
J	Jacobian
k	arbitrary constant
M	Mach number
m	distance in meters
N	force in Newtons
$\hat{n}$	surface normal
O	characteristic location
p	pressure
R	gas constant
s	entropy
T	temperature

t	time
U	vector of independent variables
U	rotor speed
u	axial velocity component
V	velocity in nonrotating frame of reference
v	tangential velocity component
υ	specific volume
W	velocity in rotating frame of reference
x	axial coordinate
x'	one-dimensional flow coordinate
y	tangential coordinate
β	damping coefficient
Δ	incremental change
γ	ratio of specific heats
ρ	density
η	transformed coordinate
ζ	transformed coordinate
1, 2, 3	turbine station number

Subscripts

a	evaluated at point A
b	evaluated at point B
CFL	related to Courant-Friedrich-Lewy condition
c	evaluated at point C
cr	condition existing at a Mach number of unity
dn	downstream condition

i	index for grid point location
JL	maximum value
j	index for grid point location
KL	maximum value
L	lower
R	relative to rotating frame of reference
t	total or stagnation condition
U	upper
up	upstream condition
x	differentiation with respect to x
y	differentiation with respect to y
η	differentiation with respect to η
ζ	differentiation with respect to ζ
∞	conditions existing in quiescent region
1, 2	state points

Superscripts

n	time level

Abstract

A numerical algorithm is developed with the capability of capturing shocks in the internal blade passages of a modern gas turbine. The algorithm uses MacCormack's explicit finite difference scheme to solve the two-dimensional form of the Euler equations. Inlet and exit boundary conditions are developed that allow disturbances to propagate out of the computational domain without reflection. Periodic boundary conditions are applied such that an infinite cascade is modeled.

The computed steady state solution is compared with experimental data for a high-work low aspect ratio turbine. The ability to obtain a reasonably accurate blade loading diagram within a practical execution time is demonstrated. Two oblique shocks, typical of those formed at the trailing edge of a transonic rotor blade, are captured. These shocks are smeared over several grid points, as expected with a shock capturing scheme, but their influence on the blade loading diagram is evident.

DEVELOPMENT OF A SHOCK CAPTURING CODE FOR USE AS A TOOL IN DESIGNING HIGH-WORK LOW ASPECT RATIO TURBINES

I. Introduction

Modern aircraft gas turbine engines have higher core engine pressures and temperatures than their predecessors. These engines require high pressure turbines with higher work output and lower corrected mass flow than earlier generation turbines (20:1). This type turbine incorporates blading with high turning, high hub-to-tip ratio, and low aspect ratio. The high hub-to-tip ratio and low aspect ratio are both detrimental to turbine efficiency. The high hub-to-tip ratio leads to boundary layer growth on the inner and outer annulus walls, while the low aspect ratio leads to secondary flow losses from turning the boundary layer through a large angle (4:267,271).

The flow field typically consists of regions of subsonic, transonic, and/or supersonic flow; with shock waves often forming in the transonic and supersonic regions. The shock waves further reduce turbine efficiency due to total pressure losses and shock-boundary layer interaction. Figure 1 is a schlieren photograph of the flow through a transonic turbine rotor cascade with an isentropic exit Mach number of 1.15. The shocks emanating from the trailing edge of the blades and the reflection from the suction

1

Schlieren visualization of flow through a linear cascade of high pressure transonic turbine rotor blades (130° turning) is shown in this photograph. A 3-color filter was aligned with the suction surface to show details of the shock-laminar boundary layer interaction. The characteristic "tramline" shocks separated by an expansion are clearly visible. Transition occurs on reattachment of the separation bubble. The isentropic outlet Mach number is 1.15, and the Reynolds number is 7×10^5 (based on chord).

The photo by J. J. Camus, Whittle Laboratory, Cambridge, U.K., is from a research program on the control of shock-boundary layer interactions sponsored by Rolls-Royce plc.

Figure 1. Typical Shock Waves in a Transonic Rotor Cascade (5).

2

surface are clearly visible, as is the presence of a separation bubble where the shock intersects the suction surface. This figure also depicts the spatial periodicity of the flow field. The present work is directed toward locating these shocks and providing the designer with a reasonably accurate blade loading diagram.

A two-dimensional solution of the time dependent Euler equations is undertaken since they provide the capability to compute mixed subsonic, transonic, and/or supersonic flows and also capture shocks. A modified version of Shang's implementation of the MacCormack scheme is used to march the solution in the time domain (19).

All computations are carried out in a reference system attached to the rotor. Figure 2 depicts a typical turbine stage with the station numbering conventions outlined in reference 12. The subscript R denotes the relative reference system, defined as the reference system moving with the rotor. Velocities in this system are given the symbol W, while velocities in the nonrotating reference system are given the symbol V. The symbol U denotes the rotational speed. A computational domain is established between two adjacent rotor blades. The domain extends upstream of station 2_R and downstream of station 3_R by approximately one-half of the rotor axial chord length. A typical grid, with 76 points in the axial direction and 33 points in the tangential direction, is shown in Figure 3.
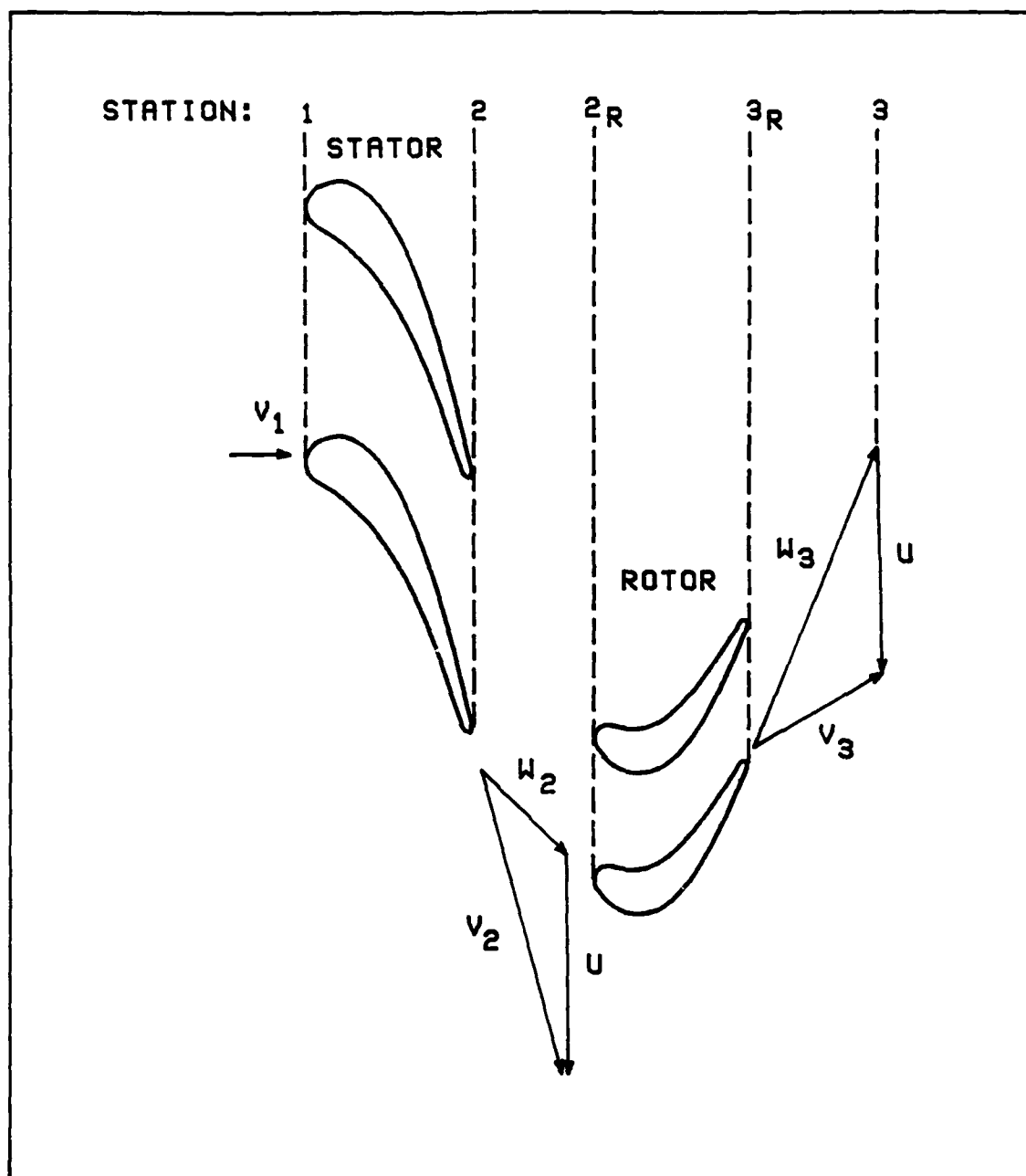
Figure 2. Turbine Stage Nomenclature

The code developed during this effort, hereafter referred to as BLD2BLD, is used to investigate three different problems with known steady state solutions. A cascade of wedges with an inlet Mach number of 2.0 and completely supersonic flow is used to demonstrate the ability of BLD2BLD to capture well defined oblique shocks. The results are compared to the exact solution presented by Denton (6:7). For the second case, BLD2BLD is used to compute the flow field in the rotor passage of a high-work low aspect ratio turbine tested in the NASA Lewis Research Center's Warm Core Turbine Test Facility (20). The loading diagram obtained from BLD2BLD is compared to the design loading diagram obtained from NASA's TSONIC code (20). The final case utilizes the NASA turbine's geometry but the exit static pressure is reduced beyond that tested by NASA. This case is thought to be representative of the conditions currently being investigated by turbine designers.
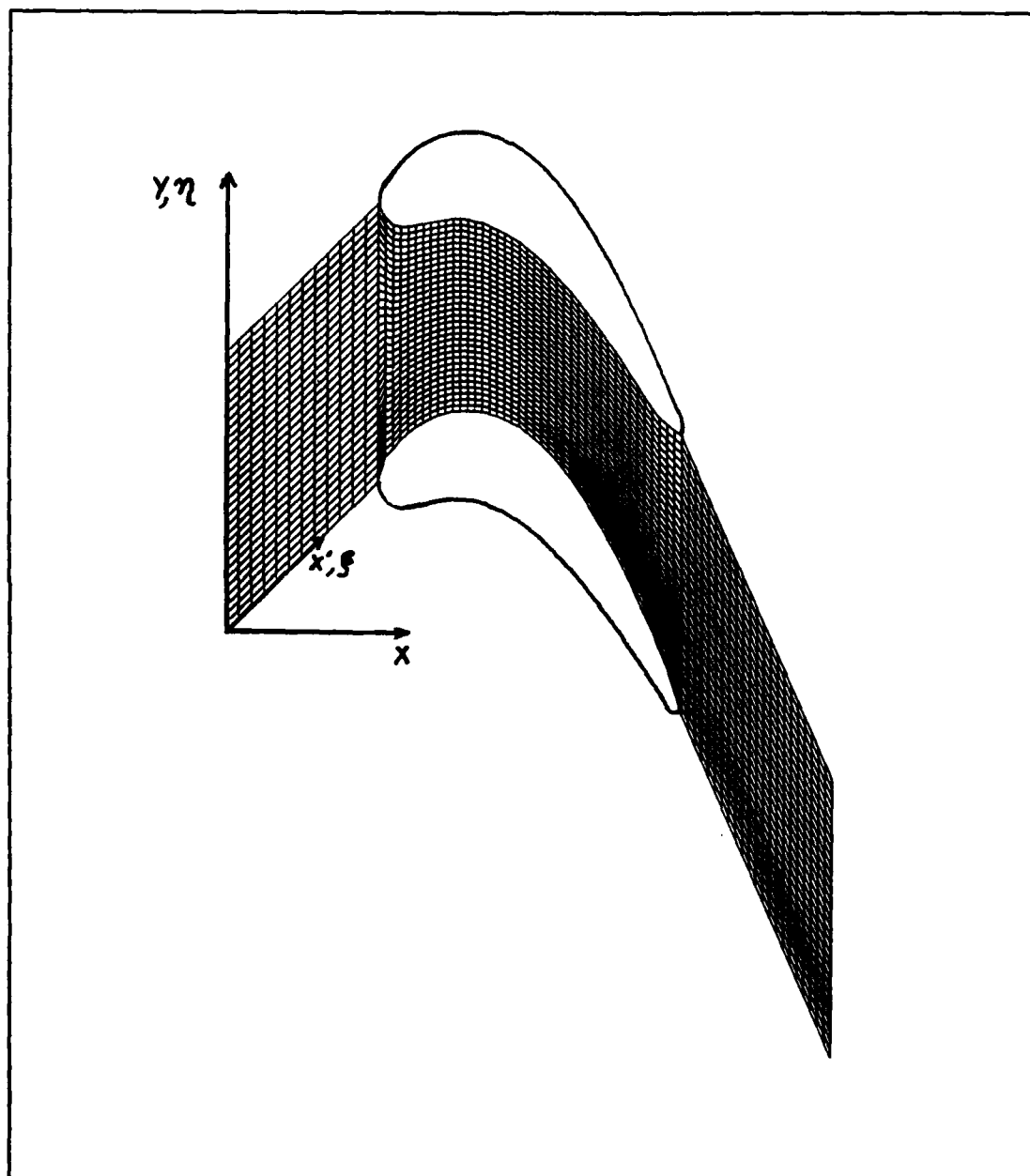
Figure 3. Typical Grid Used in the Present Analysis

II. Analysis

The present section provides a synopsis of the governing equations and boundary conditions applied in the BLD2BLD code. The Euler equations are written in conservative form and their applicability to shock capturing is discussed. A coordinate transformation is then applied to facilitate the numerical solution and application of boundary conditions. Next, the appropriate boundary conditions for flow through a blade passage are developed. These boundaries are the radiative boundaries at the inlet and exit, the periodic fluid boundaries, and the blade surfaces.

Governing Equations

The Euler equations are statements of the conservation laws for mass, momentum, and energy assuming an inviscid nonconducting gas. The favorable pressure gradient and high Reynold's number in an axial flow turbine make the Euler equations an attractive alternative to the Navier-Stokes equations as long as heat transfer or skin friction data are not desired. The customary forms of the conservation laws for mass, momentum, and energy in the absence of body forces are

$$\frac{D\rho}{Dt} + \rho(\nabla \cdot \underline{W}) = 0 \tag{1}$$

$$\rho \, \frac{D}{Dt}(\underset{\sim}{W}) = -\nabla p \tag{2}$$

$$\rho \, \frac{De}{Dt} + p(\nabla \cdot \underset{\sim}{W}) = 0 \tag{3}$$

where ρ is the density, $\underset{\sim}{W}$ is the velocity vector, p is the pressure, e is the internal energy per unit mass, and $\frac{D}{Dt}$ is the substantial or total derivative given by

$$\frac{D}{Dt} = \frac{\partial}{\partial t} + \underset{\sim}{W} \cdot \nabla \tag{4}$$

The symbol $\underset{\sim}{W}$ is used as a reminder that the governing equations are written in a frame of reference attached to the rotor. When Eqs (1), (2), and (3) are expanded using Eq (4) and rearranged such that ρ, ρu, ρv, and E_t are the dependent variables the conservative or divergence form of the governing equations is obtained. The symbols u and v denote components of the velocity vector, $\underset{\sim}{W}$, in the x and y directions defined by a Cartesian coordinate system. E_t is defined to be the total energy per unit volume given by

$$E_t = \rho \left[e + u^2/2 + v^2/2 \right] \tag{5}$$

Roache states that the conservative form of the governing equations for inviscid compressible flow was given by Courant and Friedrichs in 1946 (15:211). Lax showed that the conservative form of the governing equations satisfies the weak solution of the Rankine-Hugoniot relations and thus correctly predicts the jump conditions across the shock

discontinuity (15:211, 3:272). In fact, use of the
conservative form is necessary for the discontinuity to
physically represent a shock wave when numerical
shock-capturing schemes are applied (3:272).

References 7 and 15 present derivations of the
conservative form of the Euler equations and such a
derivation will not be repeated here. The results will
simply be stated and placed in vector form as given in
reference 3.

Eq (1) is already in conservative form which is
apparent when Eq (4) is used to expand the substantial
derivative. Some manipulation of Eqs (2) and (3) is
necessary to obtain their conservative forms with the end
result being, for two-dimensional flow

$$\frac{\partial \rho}{\partial t} + \frac{\partial}{\partial x}(\rho u) + \frac{\partial}{\partial y}(\rho v) = 0 \qquad (6)$$

$$\frac{\partial}{\partial t}(\rho u) + \frac{\partial}{\partial x}(\rho u^2 + p) + \frac{\partial}{\partial y}(\rho uv) = 0 \qquad (7)$$

$$\frac{\partial}{\partial t}(\rho v) + \frac{\partial}{\partial x}(\rho uv) + \frac{\partial}{\partial y}(\rho v^2 + p) = 0 \qquad (8)$$

$$\frac{\partial}{\partial t}(E_t) + \frac{\partial}{\partial x}\left[(E_t + p)u\right] + \frac{\partial}{\partial y}\left[(E_t + p)v\right] = 0 \qquad (9)$$

The conservative form is often referred to as the
divergence form because the equations identify the
divergence of physical quantities (3:50). This structure
allows the governing equations to be written in vector form:

$$\frac{\partial U}{\partial t} + \frac{\partial E}{\partial x} + \frac{\partial F}{\partial y} = 0 \qquad (10)$$

9

where U contains the dependent variables, E contains the terms differentiated with respect to x, and F contains the terms differentiated with respect to y. The elements of U, E, and F are:

$$U = \begin{bmatrix} \rho \\ \rho u \\ \rho v \\ E_t \end{bmatrix} \qquad E = \begin{bmatrix} \rho u \\ \rho u^2 + p \\ \rho u v \\ (E_t + p)u \end{bmatrix} \qquad F = \begin{bmatrix} \rho v \\ \rho u v \\ \rho v^2 + p \\ (E_t + p)v \end{bmatrix}$$

The governing equations are more easily solved in a rectangular uniformly-spaced computational domain than in a nonrectangular physical domain with nonuniform spacing. Thus, the governing equations need to be transformed from a Cartesian coordinate system to a general coordinate system. The general spatial transformation

$$\zeta = \zeta(x,y) \tag{11}$$

$$\eta = \eta(x,y) \tag{12}$$

is used to transform Eq (10) from the physical domain (x,y) to the computational domain (ζ,η). The partial derivatives in the physical domain become

$$\frac{\partial}{\partial x} = \zeta_x \frac{\partial}{\partial \zeta} + \eta_x \frac{\partial}{\partial \eta} \tag{13}$$

$$\frac{\partial}{\partial y} = \zeta_y \frac{\partial}{\partial \zeta} + \eta_y \frac{\partial}{\partial \eta} \tag{14}$$

where the subscripts x any y denote differentiation with

10

respect to x or y. The terms ζ_x, ζ_y, η_x, and η_y are known as metrics. The Jacobian of the transformation given by Eqs (11) and (12) is

$$J(\zeta,\eta) = \frac{\partial(\zeta,\eta)}{\partial(x,y)} = \begin{vmatrix} \zeta_x & \zeta_y \\ \eta_x & \eta_y \end{vmatrix} \qquad (15)$$

The Jacobian is evaluated as follows:

$$J = 1/J^{-1} = 1/ \begin{vmatrix} x_\zeta & x_\eta \\ y_\zeta & y_\eta \end{vmatrix} = 1/ \left(x_\zeta\, y_\eta - x_\eta\, y_\zeta \right) \qquad (16)$$

where the subscripts ζ and η denote differentiation with respect to ζ or η. The differentiations are carried out using finite difference representations since analytical expressions are not available (3:254). The metrics are determined from the relations

$$\zeta_x = J\, y_\eta \qquad (17)$$

$$\zeta_y = -J\, x_\eta \qquad (18)$$

$$\eta_x = -J\, y_\zeta \qquad (19)$$

$$\eta_y = J\, x_\zeta \qquad (20)$$

Applying this generalized transformation to the governing equations in vector form, Eq (10), results in

$$U_t + \zeta_x E_\zeta + \eta_x E_\eta + \zeta_y F_\zeta + \eta_y F_\eta = 0 \qquad (21)$$

A numerical solution is sought for the governing equations in the above form.

11

Boundary and Initial Conditions

The Euler equations, given in vector form in Eq (10), are hyperbolic for all flow regimes as long as the time-dependent terms are retained. This hyperbolic behavior requires that both boundary and initial conditions be specified. The importance of boundary and initial conditions in the solution of partial differential equations (PDE's) has been commented on by Roache:

> A first-order *ordinary* differential equation such as $df/dx = 0$ specifies the solution of a problem up to an additive constant; the boundary condition determines the value of the *constant*. A first-order *partial* differential equation such as $\partial f(x,y)/\partial x = 0$ specifies very little of the solution; any function $g(y)$ satisfies the PDE, and the boundary conditions must specify the *function*. A PDE such as $\nabla^2 \psi = \zeta$ [ψ is the stream function and ζ is the vorticity] really contains very little information on ψ. All the fantastic flow patterns of common gases and liquids are solutions of the *same* PDE's, the Navier-Stokes equations. The flows (solutions) are distinguished only by boundary and initial conditions, and by the flow parameters such as Re [Reynold's number] (15:139).

Roach suggests that the most difficult boundary condition in compressible flow occurs at a simple wall (15:261). However, for internal flows the most difficult boundary conditions occur at the inlet and exit of the passage when the flow is subsonic at one or both of these locations. Also, the periodic boundary conditions required for an infinite cascade model are a formidable challenge. The boundaries that must be dealt with are shown in Figure 4.

Radiative Boundary Conditions. The current effort is directed towards achieving a steady state solution in the
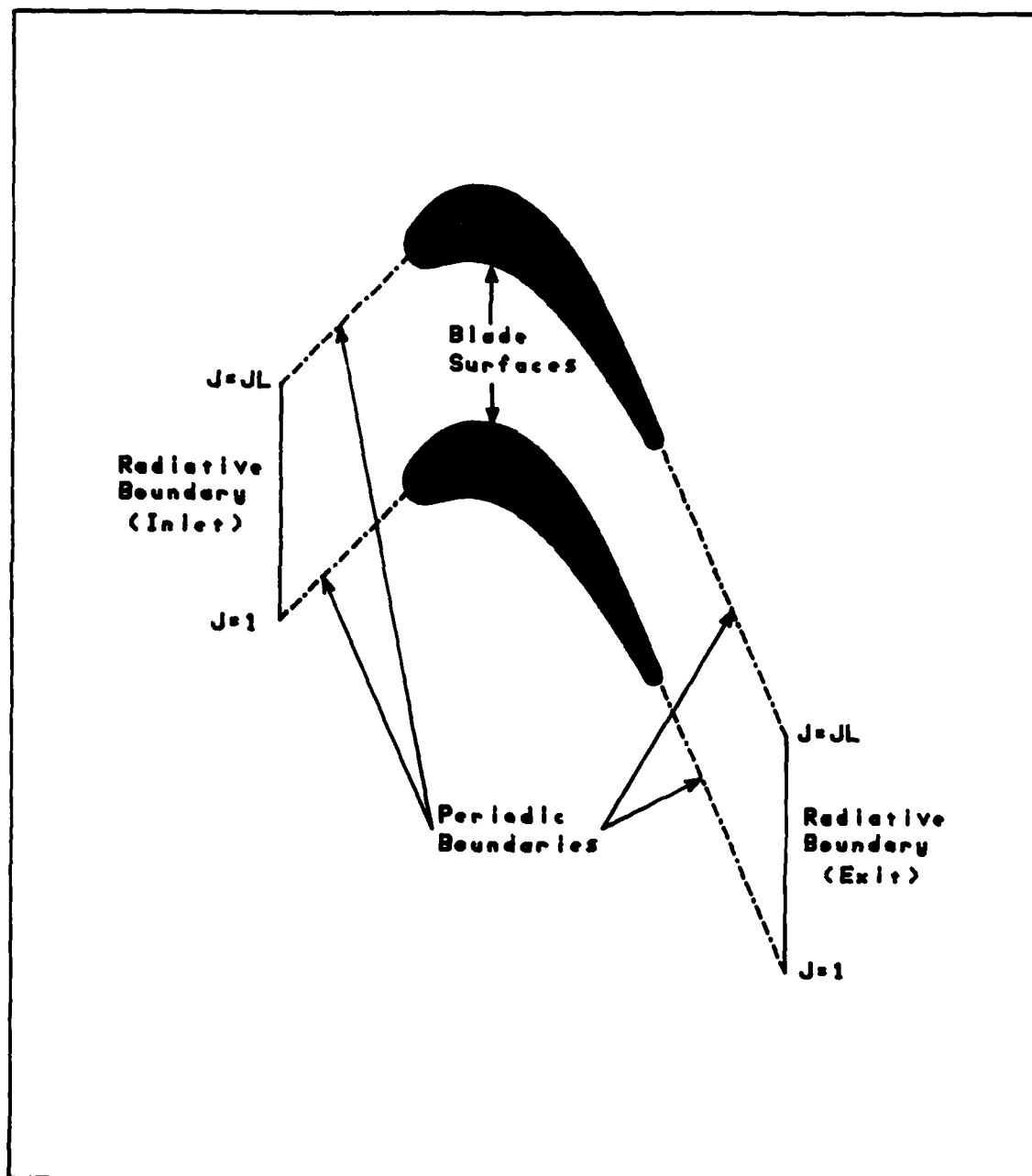
Figure 4. Physical Boundaries

13

rotor passage. Unsteady behavior due to interaction between the stator and rotor blade rows is not considered. Since Eq (10) is hyperbolic it exhibits wave behavior (7:161). All waves radiating outward from inside the computational domain should pass the inlet or exit without being reflected. This requirement is met by recasting the governing equations into characteristic form and applying simple wave theory.

Erdos and Alzner (8:21-33) and Scott and Hankey (16:144-145) report use of the method of characteristics to propagate disturbances out of the computational domain. However, Scott and Hankey only applied the method at the upstream boundary. They dealt with a compressor cascade having a supersonic relative velocity entering the rotor with the axial flow remaining subsonic. The relative velocity exiting the rotor was subsonic. They inserted a convergent-divergent nozzle downstream of the exit to achieve supersonic flow so that supersonic flow conditions could be applied at the outflow boundary (16:145). The insertion of a convergent-divergent nozzle downstream of the rotor, while a novel solution for the compressor problem, limits the exit flow from the rotor to subsonic velocities. Modern high-work turbines often have supersonic exit velocities. To allow generalization of the current work to both subsonic and supersonic exit velocities, simple wave theory is applied herein.

Erdos and Alzner state,

> The characteristic surfaces formed by the
> hyperbolic system of differential equations . . .
> consist of a conoid with its base on the x,y plane and
> within it a stream path which intersects the conoid at
> its vertex. If the vertex is placed at a grid point at
> time t+Δt, the base covers the domain of dependence of
> the point at time t (8:22).

A more manageable approximation of the above two-dimensional
characteristic theory is obtained when the characteristic
surfaces are replaced by characteristic curves. This yields
the familiar one-dimensional characteristic directions shown
in Figure 5 (8:23). The inlet and exit variables that are
not directly specified as boundary conditions are updated
using the compatibility relations, or Riemann invariants,
that are valid along the appropriate characteristics.
The characteristics AO and CO shown in Figure 5 are wave
paths while the remaining characteristic, BO, is the
particle path. The wave paths are given by

$$\frac{dx}{dt} = u + a \tag{22}$$

$$\frac{dx}{dt} = u - a \tag{23}$$

where a is the local speed of sound. The remaining equation
is that of the particle path:

$$\frac{dx}{dt} = u \tag{24}$$

Referencing Erdos and Alzner (8:22), some discussion of
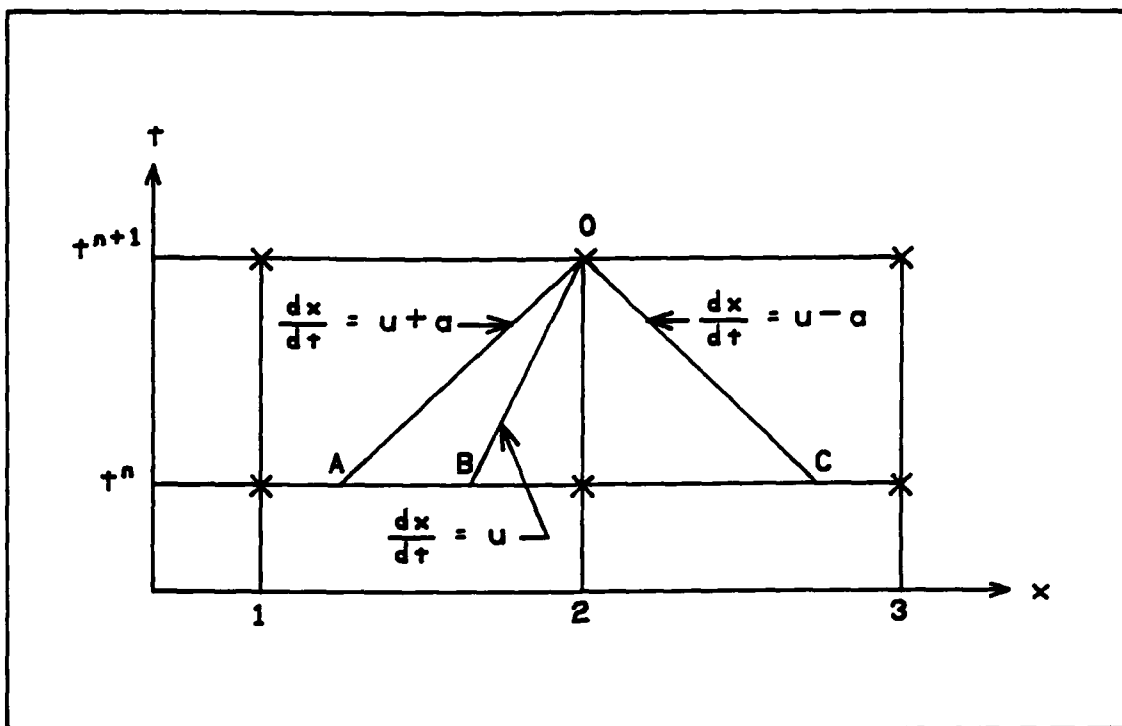the characteristic directions is in order. If Station 2 is

Figure 5. Characteristic Directions

the inlet plane, Station 3 lies inside the computational
domain and Station 1 does not exist. Only one
characteristic, CO in Figure 6a, lies inside the domain to
relate the conditions at t^{n+1} to the known conditions at t^n.
Three boundary conditions, described later, must be
specified at the inlet. One of these boundary conditions
replaces the compatibility relation along the wave path
upstream of the inlet. The other two conditions replace the
characteristic along the particle path. The above
statements apply when the Mach number at the inlet is
subsonic. If the Mach number at the inlet were supersonic,
all characteristics would originate upstream of the inlet
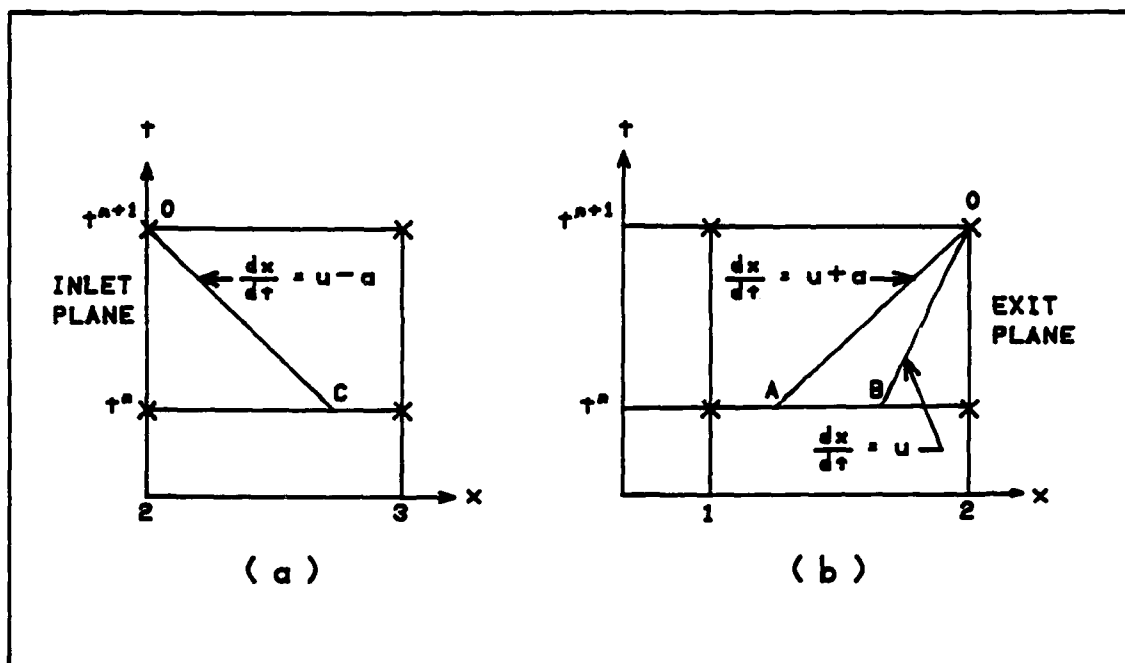
Figure 6. Applicable Characteristics at Inlet and Exit

and the solution at this boundary would be known.
Similarly, if Station 2 is the exit plane, Station 1
lies inside the computational domain and Station 3 does not
exist. Two characteristics, AO and BO in Figure 6b, lie
inside the domain to relate conditions at t^{n+1} to the known
conditions at t^n. Only one boundary condition at the exit
can be specified, replacing the compatibility relation along
the wave path downstream.

Particle Path Characteristics. For an inviscid
adiabatic flow in the absence of shocks, an alternate form
of the energy equation written along the particle path is

$$\frac{Ds}{Dt} = 0 \qquad\qquad (25)$$

17

where s is the entropy (7:31). Integration of Eq (25) along the particle path given by Eq (24) yields $s =$ constant . Thus the compatibility relation along the particle path can be written as

$$p/\rho^\gamma = \text{constant} \tag{26}$$

Wave Path Characteristics. The derivation of the wave path characteristics follows the outline given by Erdos and Alzner (8:25-28). For clarity, the equation of state that Erdos and Alzner begin with will be derived. This equation of state relates pressure to the state variables density and entropy. The starting point is the Gibbs equation:

$$Tds = de + pd\nu \tag{27}$$

where T is the temperature and ν is the specific volume. The static enthalpy, h, is by definition

$$h = e + p\nu \tag{28}$$

thus

$$de + pd\nu = dh - \nu dp \tag{29}$$

Eq (29) is substituted into Eq (27) giving

$$Tds = dh - \nu dp \tag{30}$$

Eq (30) is rewritten using the equation of state, $P = \rho RT$, and the differential form of enthalpy for a perfect gas,

18

$dh = C_p dT$, to obtain

$$ds = C_p dT/T - R \, dp/p \qquad (31)$$

where C_p is the specific heat at constant pressure and R is the gas constant. For a calorically perfect gas, Eq (31) is integrated between states 1 and 2 to give

$$\Delta s/R = \ln\left[\left(T_2/T_1\right)^{\frac{\gamma}{\gamma-1}}\left(p_1/p_2\right)\right] \qquad (32)$$

where $\Delta s = s_2 - s_1$ and γ is the ratio of specific heats. Emanuel then performs the substitution (7:17)

$$s_1/R = -\ln\left[\rho_1/T_1^{1/(\gamma-1)}\right] + \text{constant} \qquad (33)$$

leading to

$$p = k\rho^\gamma \exp\left[s/C_v\right] \qquad (34)$$

where k is a constant and the state 2 subscript has been dropped. Eq (34) is the state equation used to initiate the derivation of the compatibility relations along the wave path characteristics.

Taking the natural logarithm of both sides of Eq (34) and differentiating the result using the substantial derivative leads to

$$1/p \, \frac{Dp}{Dt} = \gamma/\rho \, \frac{D\rho}{Dt} + 1/C_v \, \frac{Ds}{Dt} \qquad (35)$$

19

where C_v is the specific heat at constant volume. Applying the definition of the substantial derivative and using the energy equation, Eq (25), gives

$$1/p \left(\frac{\partial p}{\partial t} + u \frac{\partial p}{\partial x} + v \frac{\partial p}{\partial y} \right) = \gamma/\rho \left(\frac{\partial \rho}{\partial t} + u \frac{\partial \rho}{\partial x} + v \frac{\partial \rho}{\partial y} \right) \tag{36}$$

The continuity equation, Eq (6), is substituted into the above relation, and the result multiplied by the speed of sound, to obtain

$$\frac{a}{\gamma p} \left(\frac{\partial p}{\partial t} + u \frac{\partial p}{\partial x} + v \frac{\partial p}{\partial y} \right) = -a \left(\frac{\partial u}{\partial x} + \frac{\partial v}{\partial y} \right) \tag{37}$$

The next step is to add and subtract the streamwise momentum equation, Eq (7), to the above relation. Eq (7) is first transformed into nonconservative form using the continuity equation:

$$\frac{\partial u}{\partial t} + u \frac{\partial u}{\partial x} + v \frac{\partial u}{\partial y} = - 1/\rho \frac{\partial p}{\partial x} \tag{38}$$

Substituting Eq (38) into Eq (37) and collecting like terms

$$\frac{a}{\gamma p} \left[\frac{\partial p}{\partial t} + (u \pm a) \frac{\partial p}{\partial x} + v \frac{\partial p}{\partial y} \right]$$

$$\pm \left[\frac{\partial u}{\partial t} + (u \pm a) \frac{\partial u}{\partial x} + v \frac{\partial u}{\partial y} \right] = -a \frac{\partial v}{\partial y} \tag{39}$$

This equation becomes an exact differential:

$$\frac{a}{\gamma p} \frac{dp}{dt} \pm \frac{du}{dt} = -a \frac{\partial v}{\partial y} \tag{40}$$

on the equations of the characteristic lines (8:26)

$$\frac{dx}{u\pm a} = \frac{dy}{v} = dt \tag{41}$$

Eq (41) represents the characteristic directions shown in Figure 5. With $ds = 0$, Eq (31) yields $\frac{dp}{p} = \frac{\gamma}{\gamma-1} \frac{dT}{T}$. Substituting this relation into Eq (40) and neglecting the term $\frac{\partial v}{\partial y}$ outside the computational domain gives

$$\frac{a}{\gamma-1} \frac{dT}{T} \pm du = 0 \tag{42}$$

Eq (42) is integrated to yield the well known Riemann invariants:

$$\frac{2a}{\gamma-1} \pm u = \text{constant} \tag{43}$$

The Riemann invariants are often referred to as integrated forms of the compatibility relations (7:163).

Determination of Inlet Boundary Conditions. The key to determining the proper boundary conditions is to treat the inlet as if it was part of a duct extending infinitely far upstream. All waves radiating from the computational domain should pass the inlet, without reflection, and continue travelling upstream for all time. As previously mentioned, if Station 2 in Figure 5 is taken to be the inlet plane then the only straight characteristic that exists is the line CO. This straight characteristic is known as a characteristic of the first kind (9). The

21

straight characteristics AO and BO do not exist since the wave is travelling upstream. However, a curved characteristic exists which extends into a quiescent region of uniform thermodynamic properties. This characteristic is known as a characteristic of the second kind (9). These characteristics intersect at point O in Figure 6a, a grid point at the inlet, at time t^{n+1}. Application of the Riemann invariants along both types of characteristics results in a system of two simultaneous equations to be solved for the variables u and a. Specification of the velocity direction at the inlet, along with the assumption of one-dimensional flow upstream and immediately downstream of the inlet, allows use of a coordinate system with axes aligned parallel and perpendicular to the flow. In this coordinate system the Riemann invariants given by Eq (43) become

$$\frac{2a}{\gamma-1} \pm W = \text{constant} \qquad\qquad (44)$$

where W is the magnitude of the velocity vector $\underset{\sim}{W}$. The benefits of the one-dimensional flow assumption immediately downstream of the inlet will become apparent when the numerical implementation of the characteristic theory is discussed in the next chapter. The two simultaneous equations are now in the variables W and a.

The procedure for determining the inlet boundary conditions starts with specification of a, W, and p in the

22

quiescent region upstream. These values are denoted by the symbols a_∞, W_∞, and p_∞. The inlet speed of sound and velocity at time t^{n+1} are related to the known speed of sound and velocity at point C at time t^n through the Riemann invariant along the upstream travelling wave:

$$\frac{2}{\gamma-1} a - W = \frac{2}{\gamma-1} a_c - W_c \qquad (45)$$

where the subscript c denotes the values at point C. Along the characteristic of the second kind

$$\frac{2}{\gamma-1} a_\infty + W_\infty = \frac{2}{\gamma-1} a + W \qquad (46)$$

Simultaneous solution of Eqs (45) and (46) for the speed of sound at the inlet results in

$$a = \frac{1}{2} \left(a_c + a_\infty \right) + \frac{\gamma-1}{4} \left(W_\infty - W_c \right) \qquad (47)$$

With the speed of sound known, the velocity is obtained from Eq (46):

$$W = \frac{2}{\gamma-1} \left(a_\infty - a \right) + W_\infty \qquad (48)$$

The pressure is obtained from the isentropic relation

$$p = p_\infty \left(a/a_\infty \right)^{\frac{2\gamma}{\gamma-1}} \qquad (49)$$

With the speed of sound and pressure known the state point

is fixed, uniquely determining the density and internal
energy.

Determination of Exit Boundary Conditions. The
development of the exit boundary conditions closely follows
that for the inlet conditions. The exit is treated as an
open-end duct that exhausts into a plenum. This requires
that the exit pressure match the plenum pressure. Again
referring to Figure 5, the characteristics AO and BO
originate inside the domain and the characteristic CO does
not exist since the wave is travelling downstream. Since
entropy is convected along particle paths (7:24), the
density is determined from the isentropic relation

$$\rho = \rho_b \left(p/p_b \right)^{1/\gamma} \tag{50}$$

where p has been specified and the subscript b denotes the
values at point B. The pressure and density fix the state
point so the temperature, hence speed of sound and internal
energy, is uniquely determined. The exit velocity is
obtained by evaluating the Riemann invariant along the
characteristic AO:

$$W = W_a - \frac{2}{\gamma-1} \left(a - a_a \right) \tag{51}$$

Lateral Boundary Conditions. Only one blade passage of
an infinite cascade is being analyzed, therefore the
conditions along the lateral boundaries must be periodic
except on the blade surfaces. Along any axis perpendicular

24

to the axial direction

$$(\rho)_1 = (\rho)_{JL} \tag{52}$$

$$(\rho u)_1 = (\rho u)_{JL} \tag{53}$$

$$(\rho v)_1 = (\rho v)_{JL} \tag{54}$$

$$(E_t)_1 = (E_t)_{JL} \tag{55}$$

where 1 denotes the lower boundary and JL denotes the upper boundary. For an inviscid flow, the only condition that can be applied along the blade surface is the requirement of surface tangency.

Initial Conditions. Two classes of initial conditions are investigated. The first class is termed a cascade tunnel start because of its analogy to the starting of an indraft cascade tunnel. The domain is initialized at the stagnation conditions associated with the quiescent region upstream of the inlet. At time t_o the exit pressure is instantaneously applied just as if a valve had been opened to a low pressure plenum downstream of the exit. The second class of initial conditions consists of using a restart file available from a previous solution. The restart file is used to initialize the domain before applying new quiescent region conditions or a new exit pressure. As an example, if solutions are desired for several different values of the exit pressure, the cascade tunnel start could be used for the highest exit pressure and then the restart file used to

25

initialize the domain for the next pressure investigated, or vice versa.

Of the two classes of initial conditions, the cascade tunnel start is perhaps the most noteworthy. It has been pointed out by Gray (9) that the cascade tunnel start is possible due to application of characteristic theory at the radiative boundaries. If the dependent variables were explicitly stated at the inlet and exit a better initial approximation of the steady state solution would be required such that large disturbances could not pass these radiative boundaries.

III. Solution Technique

The time-dependent Euler equations, given in vector form as Eq (21), are hyperbolic with respect to time. This hyperbolic nature allows the solution to be marched in time even though the flow may consist of mixed subsonic, transonic, and/or supersonic regions (3:259). The numerical technique used to obtain a solution of the Euler equations for steady flow in a turbine cascade is discussed in this chapter. Details of the finite differencing scheme and numerical implementation of the boundary conditions are covered. Stability and convergence, allowable time step size, and numerical damping are also mentioned.

Finite Difference Scheme

MacCormack's explicit finite difference scheme is used to obtain a time marching solution of the Euler equations (21). The BLD2BLD code is a modified version of Shang's three-dimensional code (17,18). The modifications were necessary to adapt the code for solution of two-dimensional internal flows. These modifications have no effects on Shang's implementation of the differencing scheme except at the lateral boundaries. MacCormack's scheme is a two-step Lax-Wendroff method. This scheme uses alternating forward and backward differences for the predictor and corrector sweeps respectively. The predictor and corrector sweeps applied to the Euler equations in a Cartesian coordinate

27

system, Eq (12), are defined as (11:151)

$$U_{i,j}^{\overline{n+1}} = U_{i,j}^n - \frac{\Delta t}{\Delta x}\left(E_{i+1,j}^n - E_{i,j}^n\right) - \frac{\Delta t}{\Delta y}\left(F_{i,j+1}^n - F_{i,j}^n\right) \qquad (56)$$

$$U_{i,j}^{n+1} = \frac{1}{2}\left[U_{i,j}^n + U_{i,j}^{\overline{n+1}} - \frac{\Delta t}{\Delta x}\left(E_{i,j}^{\overline{n+1}} - E_{i-1,j}^{\overline{n+1}}\right)\right.$$
$$\left. - \frac{\Delta t}{\Delta y}\left(F_{i,j}^{\overline{n+1}} - F_{i,j-1}^{\overline{n+1}}\right)\right] \qquad (57)$$

where $E_{i,j}^n$ and $F_{i,j}^n$ equal $E\left(U_{i,j}^n\right)$ and $F\left(U_{i,j}^n\right)$. The subscripts i and j denote a mesh of points $\left(x_i, y_j\right)$ with uniform spacing Δx and Δy. The superscript n refers to the time $t = n\Delta t$ where Δt is the time increment for one predictor-corrector cycle. Finally, the overbar denotes predicted quantities. MacCormack points out that using a forward difference for the predictor and a backward difference for the corrector represents only one of four possible differencing methods (11:151). In this effort only the variation given by Eqs (56) and (57) is implemented.

The code achieves maximum efficiency by utilizing the Courant-Friedrich-Lewy (CFL) condition derived by Shang from a stability analysis (18:4):

$$\Delta t_{CFL} = 1 \Big/ \left\{ \frac{u_\zeta}{\Delta\zeta} + \frac{u_\eta}{\Delta\eta} + a\left[\left(\frac{\zeta_x}{\Delta\zeta} + \frac{\eta_x}{\Delta\eta}\right)^2\right.\right.$$
$$\left.\left. + \left(\frac{\zeta_y}{\Delta\zeta} + \frac{\eta_y}{\Delta\eta}\right)^2\right]^{1/2}\right\} \qquad (58)$$

28

where Δt_{CFL} is the allowable time step size and u_ζ and u_η are the contravariant velocities defined as

$$u_\zeta = \zeta_x u + \zeta_y v \tag{59}$$

$$u_\eta = \eta_x u + \eta_y v \tag{60}$$

The CFL condition requires that the physical domain of dependence lie within the numerical domain of influence. The numerical domain can be larger, but not smaller, than the physical domain (3:76). Anderson reports that hyperbolic systems tend to behave best when the numerical and physical domains of influence are nearly equal (3:77). The CFL numbers used in the present work ranged from 0.2 to 0.8, with 0.8 used most often. Satisfaction of the CFL condition is necessary for stability of the MacCormack scheme. Lax's equivalence theorem equates stability and convergence of a consistent finite difference scheme, for a linear system of equations (3:49). This theorem has never been proven for nonlinear equations, such as the Euler equations, but this work proceeds under the assumption that the theorem applies.

Explicit numerical damping is applied to suppress numerical oscillations. The damping is applied in each sweep direction using Shang's modification of MacCormack's fourth-order pressure damping terms (17:1349):

$$\beta \, \Delta t \, \Delta \zeta^2 \left[|u_\zeta| + \left(\zeta_x^2 + \zeta_y^2 \right)^{1/2} a \right] \frac{1}{p} \left| \frac{\partial^2 p}{\partial \zeta^2} \right| \tag{61}$$

$$\beta \ \Delta t \ \Delta \eta^2 \left[|u_\eta| + \left(\eta_x^2 + \eta_y^2 \right)^{1/2} a \right] \frac{1}{p} \left| \frac{\partial^2 p}{\partial \eta^2} \right| \tag{62}$$

where β is the damping coefficient. In the present work a damping coefficient of 2 is consistently used.

Implementation of Boundary Conditions

Attention is now focused on the numerical implementation of the boundary conditions developed in the previous chapter. The only boundaries that require additional computations beyond the predictor-corrector differencing are the inlet and exit. The conditions at the lateral boundaries, both the periodic boundaries and the blade surfaces, are obtained with modifications of the predictor-corrector differencing scheme.

Radiative Boundaries. The simple wave theory used to determine the appropriate values of the dependent variables at the inlet and exit was developed in Chapter II. The numerical implementation of this theory is the subject of this section. Referring again to Figure 6a, if station 2 is the inlet plane the conditions at any node point at time t^{n+1} is related to conditions at point C at time t^n through the Riemann invariants, Eq (45). The conditions at any inlet node point are similarly related to conditions in the quiescent region upstream through Eq (46). The speed of sound, velocity, and static pressure in the quiescent region are specified as inputs to the code. The conditions at

30

point C thus need to be determined in order to evaluate the conditions at the inlet. This is the point where the one-dimensional flow assumption immediately downstream of the inlet becomes advantageous. A coordinate system is aligned with the flow direction at the inlet such that one axis, denoted X', is aligned with the flow. By construction this axis is also aligned along a line of η, hence the j index, equal to a constant as shown in Figure 3. This construction allows the equation of the characteristic, Eq (23), to be written as

$$dx'_C/dt = W_C - a_C \tag{63}$$

Point x'_C is located through an iterative solution of the equation obtained by integrating Eq (63):

$$x'_C = x'_{inlet} - \left(W_C - a_C \right) \Delta t \tag{64}$$

with linear interpolation used to determine the flow properties at point C. The code uses the Newton-Raphson method (10:764) to perform the iterative solution of Eq (64). In addition, bisection is used as a fail-safe whenever the Newton-Raphson method would take the solution out of bounds (14:258). Once point C is located and the flow properties obtained, Eqs (47)-(49) are used to determine the flow properties at the inlet.

The exit boundary conditions are implemented in a similar fashion to those at the inlet. Referring to

31

Figure 6b, if station 2 is taken as the exit plane the characteristics AO and BO are available to relate conditions inside the domain at time t^n to exit conditions at time t^{n+1}. After applying a one-dimensional flow assumption immediately upstream of the exit the characteristic equations become

$$x'_A = x'_{exit} - \left(W_A + a_A \right)\Delta t \tag{65}$$

and

$$x'_B = x'_{exit} - W_B \Delta t \tag{66}$$

Points A and B are located through an iterative solution of Eqs (65) and (66) with linear interpolation used to determine the flow properties. With the exit pressure, P_e, given as input to BLD2BLD the exit boundary conditions are determined using Eqs (50) and (51).

Lateral Boundaries. The flow properties along the lateral boundaries are not explicitly specified but rather are determined using slightly modified forms of the MacCormack scheme. Along the periodic boundaries the conditions given by Eqs (52)-(55) are met by actually performing the predictor and corrector sweeps at the boundary. If a forward predictor is applied at the upper boundary, denoted by JL, the flow properties at $j = JL + 1$ are needed. Since this line of points does not exist when only one blade passage of an infinite cascade is being modeled, the properties at $j = JL + 1$ are replaced by the

32

conditions at $j = 2$. An analogous procedure is followed when a backward predictor is applied at the lower boundary. If the lower boundary is denoted by $j = 1$, the conditions at $j = 0$ are replaced by the condition at $j = JL - 1$. This differencing procedure appears to satisfy the periodicity requirement up to approximately one point away from the leading and trailing edges.

The appropriate boundary condition along the blade surfaces is the surface tangency requirement, $\underset{\sim}{W} \cdot \hat{n} = 0$, where $\hat{n}$ is the surface normal (15:261). The MacCormack scheme is applied directly at the blade surface, using forward differences for both the predictor and corrector on the suction surface and backward differences for both sweeps along the pressure surface. Differencing in the same direction for both the predictor and corrector is usually unstable, but Anderson points out that the surface tangency condition affects the solution such that stability is maintained (3:277).

Solutions to a variety of test cases were attempted prior to attempting the solution for an infinite cascade. These test cases ranged from fully subsonic flow through a curved duct to fully supersonic flow through a duct with surface discontinuities to generate shock and expansion waves. The above boundary conditions, less the periodicity constraint, were applied to the test cases with excellent results.

Numerical difficulties are encountered at the periodic downstream boundaries if the cascade tunnel start is used. A similar difficulty was observed by Scott and Hankey (16:146). They alleviated the problem by treating the downstream lateral boundaries as solid surfaces until the solution evolved to a point that the flow became aligned with the channel (16:146). The same remedy is applied to the current effort, eliminating the difficulties.

IV. Results and Conclusions

Results

This section describes the results obtained when the
BLD2BLD code is applied to three different test cases. The
first solution is for a cascade of wedges with an inlet Mach
number of 2.0 and supersonic flow throughout the passage. A
solution is then obtained for the NASA high-work low aspect
ratio turbine rotor described in reference 20.   The NASA
turbine geometry is used for the third solution but the exit
pressure is dropped below that of the NASA tests. This
results in a supersonic exit Mach number typical of that
currently under consideration by turbine designers.

Case One. Cascade of Wedges. The cascade of wedges
presented by Denton is used to demonstrate the ability of
BLD2BLD to capture well defined oblique shocks (6:7). This
cascade is shown in Figure 7. The cascade has an inlet Mach
number of 2.0 and is designed such that the leading edge
shock is exactly canceled upon reflection to the upstream
corner resulting in uniform flow between the two parallel
surfaces. The grid used consists of 125 points in the
axial direction and 26 points in the tangential direction.
The computed static pressure contours are shown in Figure 8.
The shock that forms at the leading edge is smeared over
several points, as is typical for a shock capturing
scheme, and is smeared even more upon reflection. As a
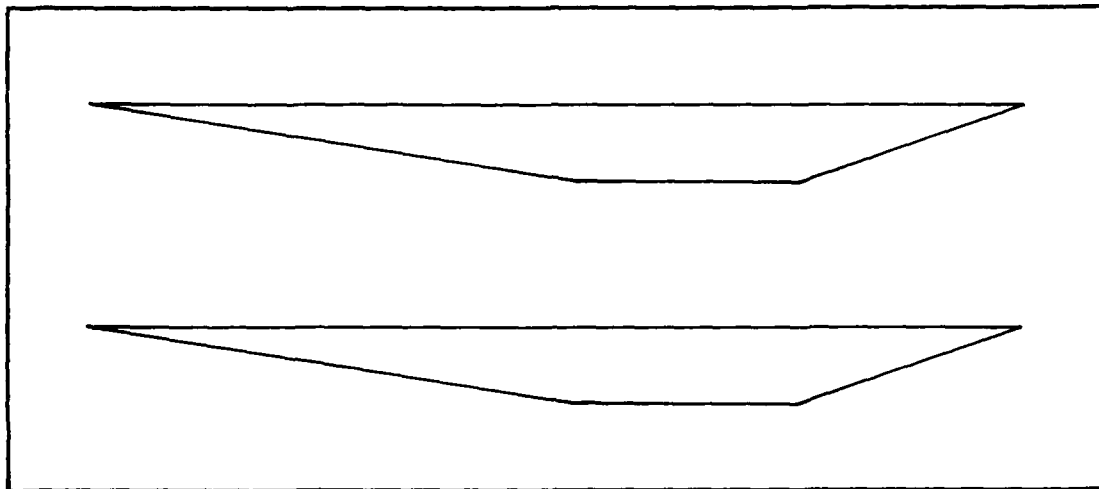
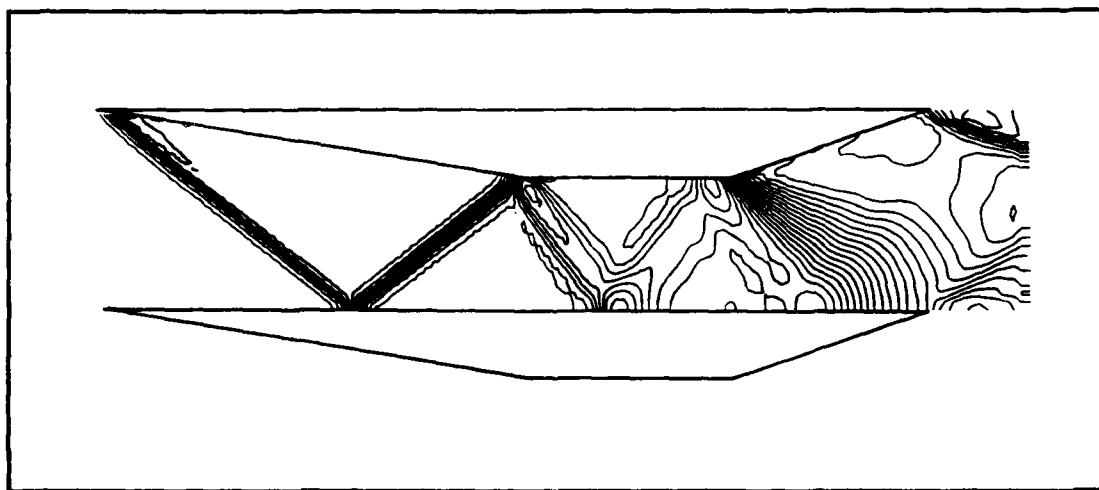Figure 7. Cascade of Wedges

Figure 8. Static Pressure Contours for Cascade of Wedges

result, the reflected shock does not exactly meet the upstream corner and a weak shock is reflected back across the passage. Additionally, a weak expansion emanates into the region between the parallel surfaces. Two oblique shock waves occur at the trailing edge, similar to the oblique shock waves occurring at the trailing edge of the turbine blades shown in Figure 1. These trailing edge shocks are a result of the periodicity conditions applied immediately downstream of the trailing edge. Figure 9 contrasts the exact and computed solutions in terms of Mach number versus the non-dimensional chord length. Numerical oscillations, or dispersive errors, occur near the points where the shock and expansion waves are generated or reflected. These dispersive errors are typical of second-order methods such as MacCormack's (3:92). The oscillations near the leading edge may also be aggravated by the periodicity conditions immediately upstream. Figure 9 also shows that the weak shock generated due to smearing intersects the lower surface near 60 percent of the chord length. An exact solution for the expansion along the lower surface was not presented by Denton. Denton attributes the exact solution to Brown Boveri & Co. of Baden, Switzerland (6:9).

Case Two. NASA High-Work Low Aspect Ratio Turbine. The BLD2BLD code is now used to obtain a steady state solution for the flow in a blade passage of an experimental turbine. The experimental turbine is a 0.767 scale model of
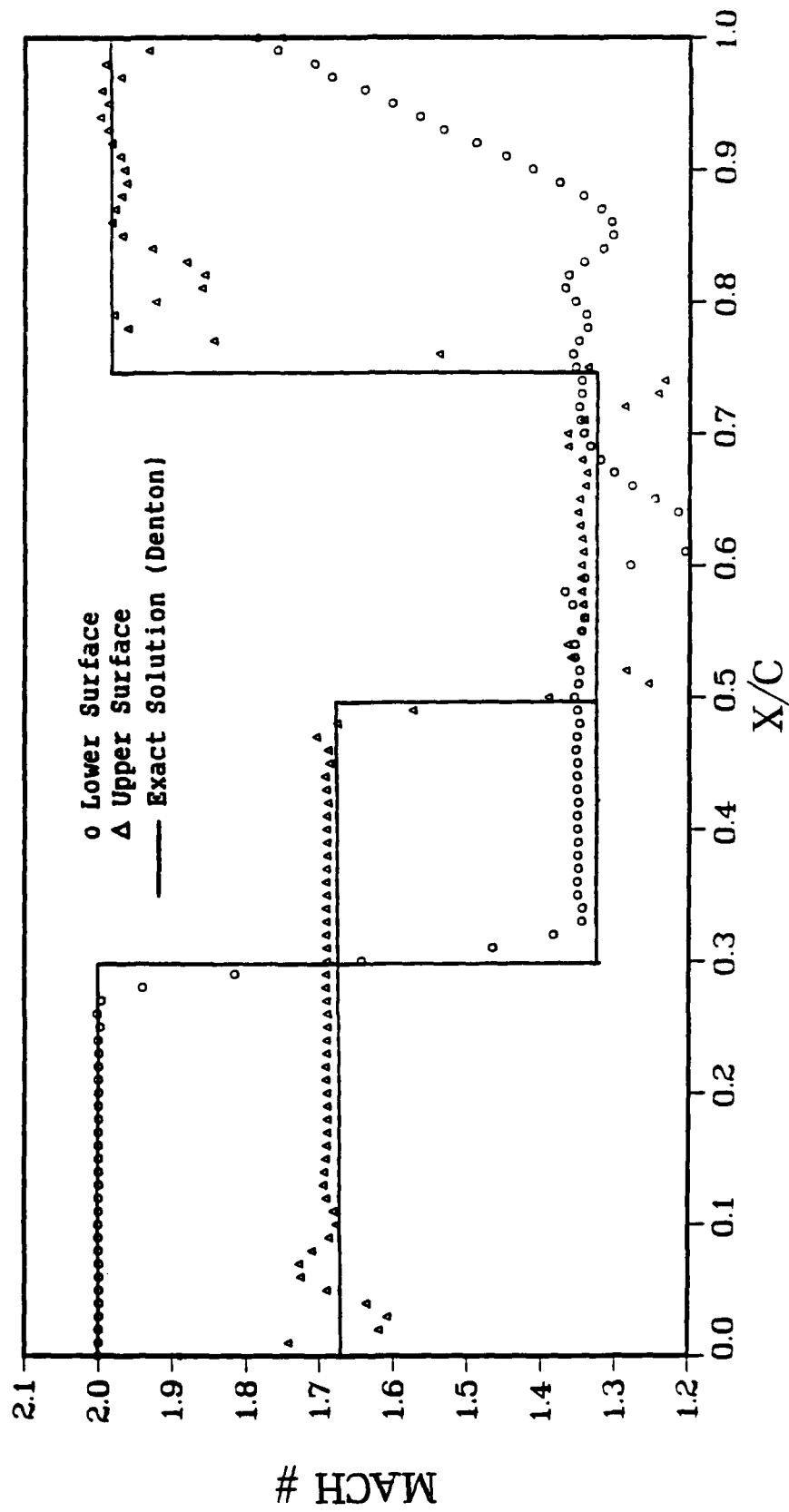
Figure 9. Blade Loading Diagram for Cascade of Wedges

the first stage of a two stage high pressure turbine

designed for use in a high bypass ratio engine. This model

was tested in the NASA Lewis Research Center's Warm Core

Turbine Test Facility and the results are well documented in

reference 20. Even though strong secondary flows

occurred in the tests (20:5), this turbine was chosen for

comparison because of the difficulty in obtaining

two-dimensional cascade data.

Figure 10 shows the mean-line velocity diagram obtained

from the NASA experiment. Using the mean-line blade

coordinates given in Table 1, and the relative gas angles

from Figure 10, the grid shown in Figure 3 is constructed.
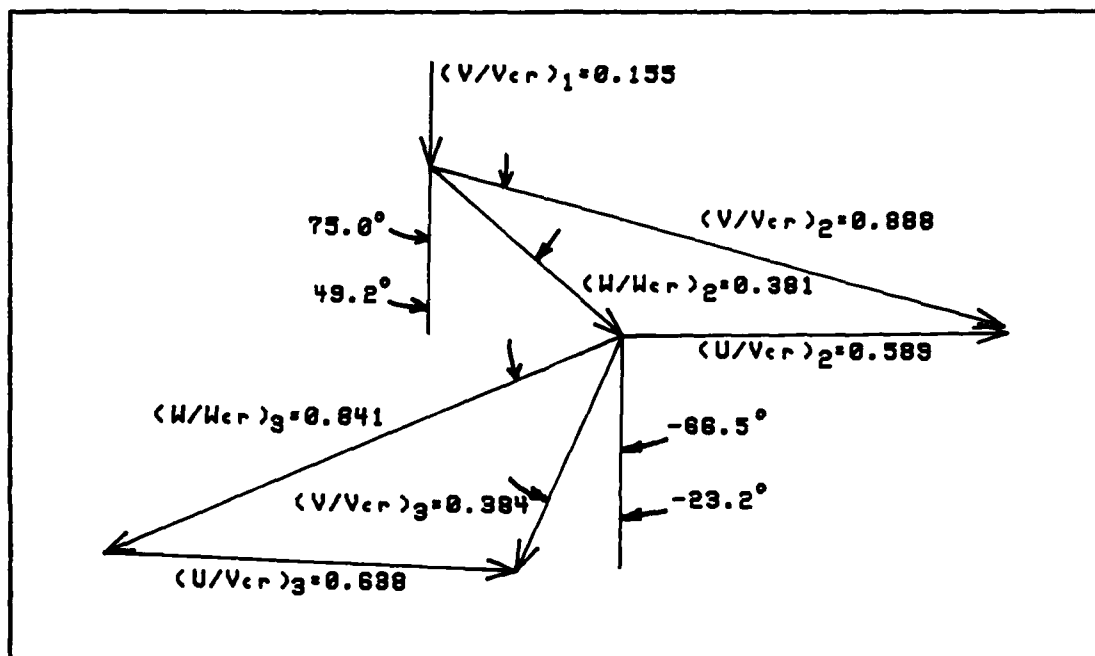
The grid consists of 76 points in the axial direction

Figure 10. Experimental Mean-Line Velocity Diagram (20:22)

Table 1. Rotor Blade Coordinates (20:8)

X	Hub		Mean		Tip	
	Stagger angle, α (deg)					
	31.74		37.93		43.20	
	Y_L	Y_U	Y_L	Y_U	Y_L	Y_U
-0.011	0.521	0.521	-----	-----	-----	-----
-0.004	-----	-----	0.441	0.441	-----	-----
0.000	0.280	0.762	0.305	0.580	0.305	0.305
0.200	0.018	1.269	0.018	1.139	0.018	0.955
0.400	0.015	1.472	0.015	1.325	0.015	1.162
0.600	0.215	1.582	0.204	1.431	0.192	1.272
0.800	0.501	1.640	0.427	1.486	0.373	1.332
1.000	0.660	1.660	0.559	1.506	0.475	1.359
1.200	0.750	1.646	0.637	1.499	0.537	1.362
1.400	0.792	1.606	0.676	1.471	0.572	1.347
1.600	0.798	1.544	0.689	1.426	0.589	1.319
1.800	0.777	1.465	0.681	1.368	0.590	1.279
2.000	0.739	1.373	0.658	1.299	0.579	1.230
2.200	0.687	1.272	0.624	1.222	0.559	1.173
2.400	0.625	1.162	0.581	1.137	0.531	1.109
2.600	0.555	1.046	0.531	1.047	0.496	1.039
2.800	0.478	0.924	0.476	0.951	0.457	0.965
3.000	0.396	0.797	0.415	0.850	0.414	0.886
3.200	0.308	0.665	0.350	0.745	0.366	0.802
3.400	0.215	0.528	0.281	0.636	0.316	0.715
3.600	0.119	0.387	0.209	0.524	0.262	0.625
3.800	0.018	0.242	0.134	0.408	0.206	0.532
3.946	0.089	0.089	-----	-----	-----	-----
4.000	-----	-----	0.056	0.290	0.148	0.437
4.200	-----	-----	0.009	0.169	0.088	0.338
4.249	-----	-----	0.089	0.089	-----	-----
4.400	-----	-----	-----	-----	0.026	0.238
4.586	-----	-----	-----	-----	0.089	0.089

and 33 points in the tangential direction. The grid
extends approximately one-half axial chord length upstream
and downstream of the blades, and the blade pitch is
3.059 cm. The lines of constant η are aligned with the
relative gas angles at each end of the grid. The blade
surface coordinates are obtained using a cubic spline
interpolation (14:86-89). In addition, the rounded trailing
edge was replaced by a sharp trailing edge for computational
purposes. The grid was generated using the algebraic
portion of Amdahl's ORTHGNL grid generation code (1).

The inlet and exit conditions necessary for input to
BLD2BLD are derived from the following NASA test
data (20:6-9, 22):

$$\gamma = 1.4 \qquad\qquad T_{t_1} = 422.2 \text{ K}$$

$$P_{t_1} = 31.03 \times 10^4 \text{ N/m}^2 \qquad P_{t_1}/P_2 = 1.704$$

$$P_{t_{2R}}/P_3 = 1.652 \qquad\qquad P_{t_1}/P_{t_3} = 2.360$$

$$(V/V_{cr})_2 = 0.888 \qquad\qquad (V/V_{cr})_3 = 0.384$$

$$(W/W_{cr})_2 = 0.381 \qquad\qquad (W/W_{cr})_3 = 0.841$$

where t identifies total properties, R denotes a frame of
reference moving with the rotor, cr is a condition
corresponding to a Mach number of unity, and the station
numbering and velocity symbols correspond to those shown in
Figure 2. Note that the test data specifies velocity ratios
rather than Mach numbers. This is a convention typically

41

followed by turbine designers. Although assumed constant for the present work, the specific heats can vary significantly through some turbines. This results in significant γ, hence Mach number, variations. Thus velocity ratios are more meaningful to the designer. The Mach number is related to the velocity ratio through the equation (2:5)

$$M^2 = \frac{2}{\gamma+1} \left(\frac{V}{V_{cr}}\right)^2 \left[1 - \frac{\gamma-1}{\gamma+1} \left(\frac{V}{V_{cr}}\right)^2\right]^{-1} \tag{69}$$

As stated in Chapter III, the speed of sound, velocity, and static pressure in the quiescent region upstream of the inlet are required as input to BLD2BLD. The speed of sound, velocity, and static pressure at station 2R, obtained from the test data, are input as the conditions existing in the quiescent region. Assuming the flow through the stator is adiabatic, the static temperature at station 2R is obtained from (2:5)

$$T_{2R} = T_{t_1} \left[1 - \frac{\gamma-1}{\gamma+1} \left(\frac{V}{V_{cr}}\right)^2_2\right] \tag{70}$$

resulting in $T_\infty = T_{2R} = 366.71$ K and $a_\infty = 383.91$ m/s . Eq (69), with V/V_{cr} replaced by W/W_{cr}, is used to arrive at $M_{2R} = 0.352$ thus giving $W_\infty = M_{2R} a_\infty = 135.14$ m/s . The static pressure is obtained directly from the given values of P_{t_1} and P_{t_1}/P_2 as $P_\infty = 18.21 \times 10^4$ N/m^2 . The static

pressure at station 3R is input to BLD2BLD as the exit
pressure, P_e. The static pressure is obtained from the
relation (2:5)

$$P_{3R} = P_{t_3} \left[1 - \frac{\gamma-1}{\gamma+1} \left(\frac{V}{V_{cr}} \right)_3^2 \right]^{\frac{\gamma}{\gamma-1}} \tag{71}$$

P_{t_3} is obtained directly from the test data giving
$P_e = P_{3R} = 12.05 \times 10^4 \ N/m^2$. All required input to BLD2BLD
is now available.

The BLD2BLD solution shows that the rotor is choked at
the throat, as shown by the Mach contours of Figure 11 and
the static pressure contours of Figure 12. The NASA test
data also suggest that the rotor was choked, or very nearly
so, at the conditions described above (20:3). The average
value of $(W/W_{cr})_2$ is slightly lower than the test data,
0.364 compared to 0.381, probably due to a slight narrowing
of the throat dimension when the blade surfaces were
numerically generated. The Mach contours of Figure 11 and
the static pressure contours of Figure 12 suggest that two
shock waves are emanating from the blade trailing edge. The
presence of these shocks is verified upon examination of
Figures 13 and 14. These figures show that the shock wave
emanating from the pressure surface strikes the suction
surface near 65 to 70 percent of the axial chord. The exact
location cannot be determined because of shock smearing. A
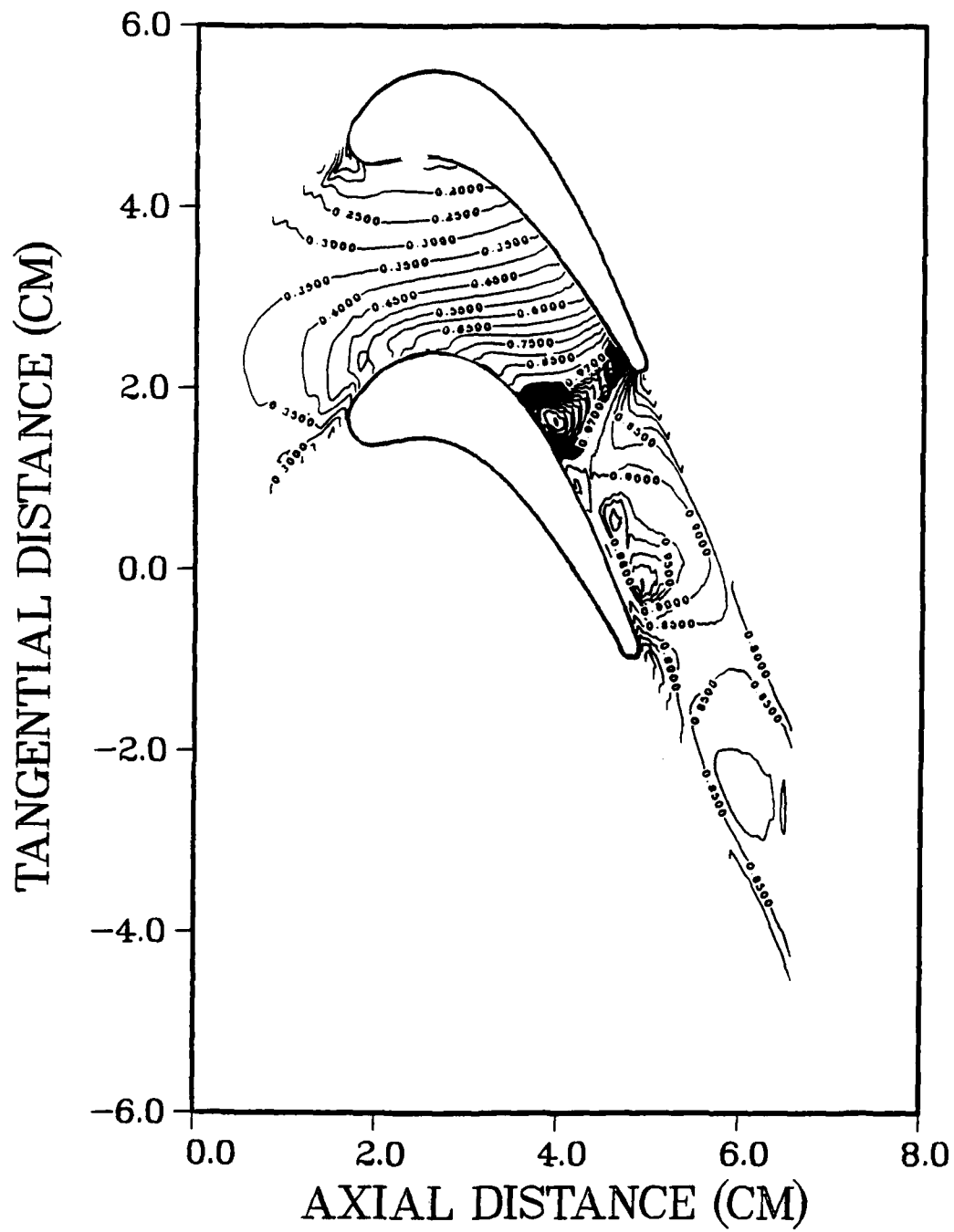reflection from the suction surface, similar to Figure 1,

43

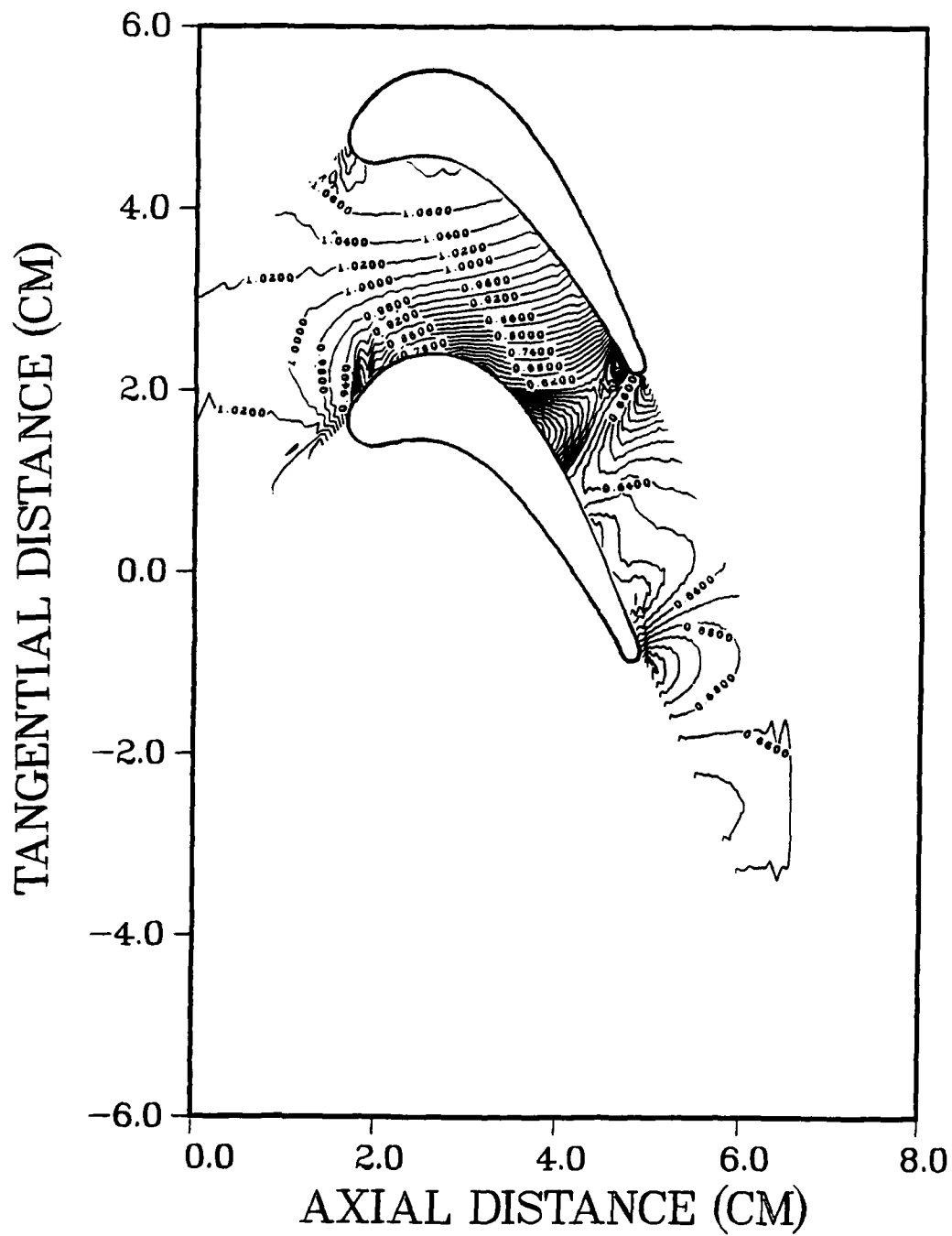**Figure 11. Mach Contours for Case Two**

44

Figure 12.   Static Pressure Contours (p/p_2) for Case Two
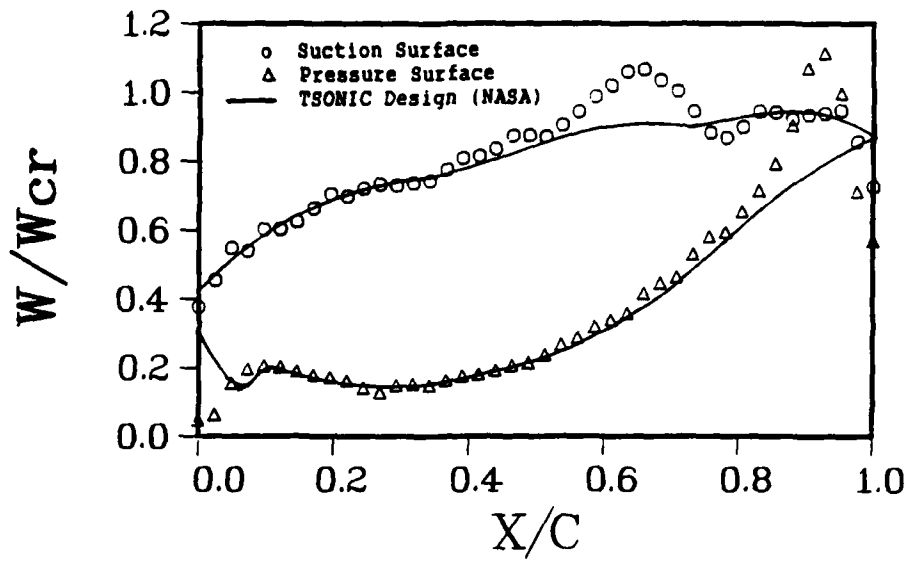
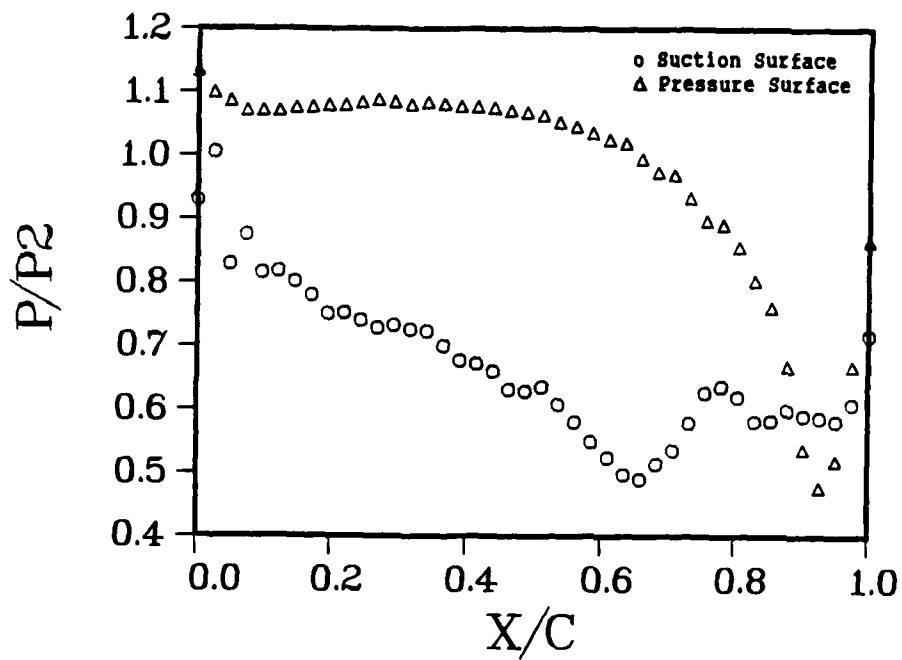Figure 13.   Blade Loading Diagram for Case Two

Figure 14.   Surface Pressures (p/p_2) for Case Two

can not be detected because of this smearing. The existence of these shocks can not be verified from the experimental data, since NASA's experimental apparatus was not equipped to sense the presence of shocks. Figures 11 and 12 also show the presence of a second shock emanating from the trailing edge of the suction surface. These shocks form because of the periodicity requirement downstream of the blade trailing edge. If the lateral boundaries upstream and downstream of the blade are treated as solid walls these trailing edge shocks are not generated. Referring to Figure 15, a normal shock then forms downstream of the throat, as verified by a solution using BLD2BLD, such that the specified exit pressure is met. The pressure is discontinuous across the normal shock, with the upstream and downstream pressures denoted by p_{up} and p_{dn} respectively. If periodicity is then applied, a pressure discontinuity exists across the stagnation streamline. The normal shock is thus replaced by two oblique shocks that align themselves such that no pressure discontinuity exists across the streamlines.

Referring again to Figure 13, the loading diagram obtained from BLD2BLD is compared with the design loading diagram obtained from NASA's TSONIC code. The two codes compare favorably except near the leading edge of the pressure surface and in the vicinity of the shock waves. Experimental measurements on transonic turbine blades,
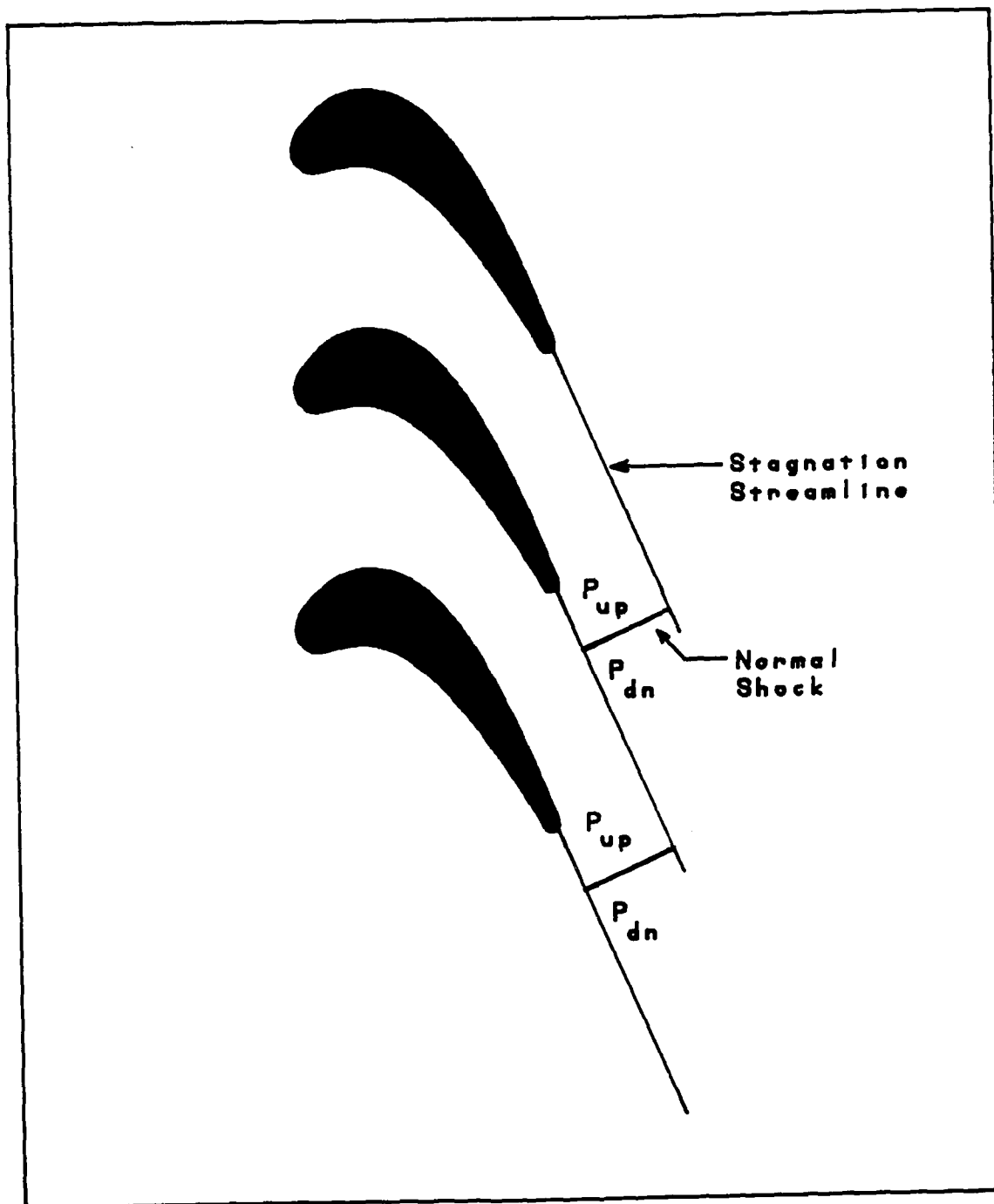
Figure 15.   Impossibility of a Normal Shock
Forming in an Infinite Cascade

presented by Denton (6:7), suggest that the BLD2BLD solution
is more representative of the blade loading near the
pressure surface leading edge. Comparisons with TSONIC can
not be made in the vicinity of the shock waves for two
reasons. First, TSONIC may have been applied to a geometry
with a slightly larger throat dimension, thus alleviating
choking. Second, there is some question in the design
community about TSONIC's ability to deal with shocks (9). A
qualitative comparison of BLD2BLD's shock capturing ability
can be made against the widely used Denton code (6). The
Denton code employs a pitchwise smoothing of the flow
properties in addition to pressure damping. This causes the
shocks to be smeared to the extent that the effect of a
shock emanating from the pressure surface is almost entirely
damped out before reaching the suction surface. Denton has
demonstrated this effect even at exit Mach numbers as high
as 1.42 (6:7). Even though BLD2BLD has a smearing effect,
as do all shock capturing schemes, the effect of a shock
impinging on the suction surface is evident from Figures 13
and 14. Examination of Figure 16 reveals a reduction in the
magnitude of the velocity vectors near the suction surface
due to a shock extending across the passage. The velocity
magnitude is further reduced as the suction surface trailing
edge shock is encountered. The average value of $\left(W/W_{cr}\right)_3$
from the BLD2BLD solution is slightly larger than the value
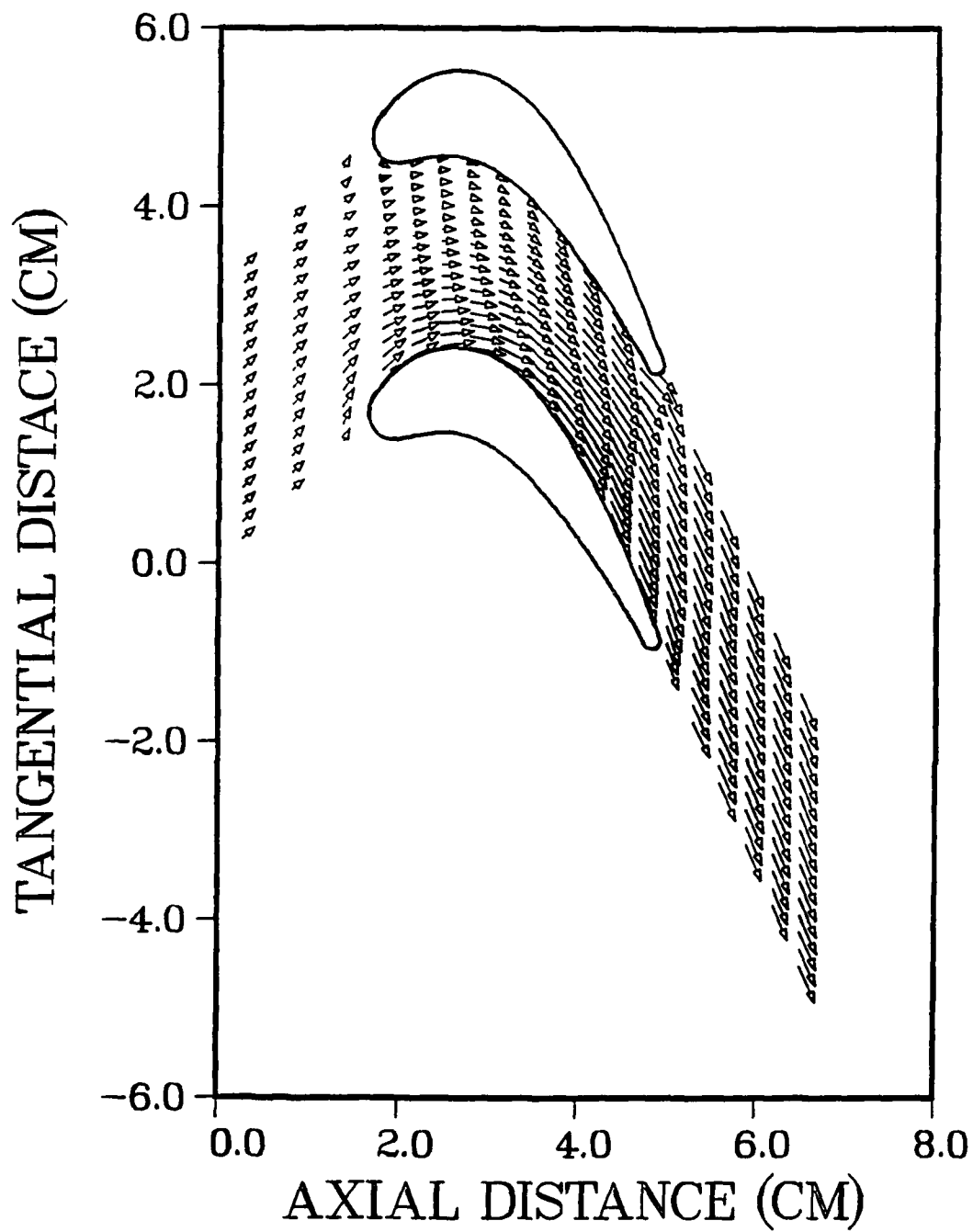obtained from the NASA test data, 0.879 using BLD2BLD

49

Figure 16. Velocity Vectors for Case Two

compared to an experimental value of 0.841. The calculated exit relative total pressure, $P_{t_{3R}}$, is also slightly larger than the experimental value, 19.53 X 10^4 N/m^2 calculated versus 18.64 X 10^4 N/m^2 experimental. This is not surprising in light of the strong secondary flows observed in the experiment.

Case Three. NASA Turbine with Lowered Exit Pressure.
This final case uses the case two geometry and inlet conditions, but the exit pressure is lowered to 8.05 X 10^4 N/m^2. The exit pressure is chosen, rather arbitrarily, such that the exit Mach number is supersonic. This case uses the same grid generated for case two. This case is thought to be representative of the conditions currently under consideration by turbine designers.

The BLD2BLD solution yields an average value of $(W/W_{cr})_3$ of 1.127 corresponding to an exit Mach number of 1.159. Figures 17 and 18 show the computed Mach and pressure contours respectively. Shock waves are again present at the trailing edges of the pressure and suction surfaces. Figures 19 and 20 show that the shock emanating from the pressure surface is somewhat stronger than for case two. The shock also impinges on the suction surface farther downstream than for the previous case. The impingement now occurs at approximately 80 percent of the axial chord. The likelihood of flow separation increases as the impingement point moves toward the trailing edge. The flow tends to
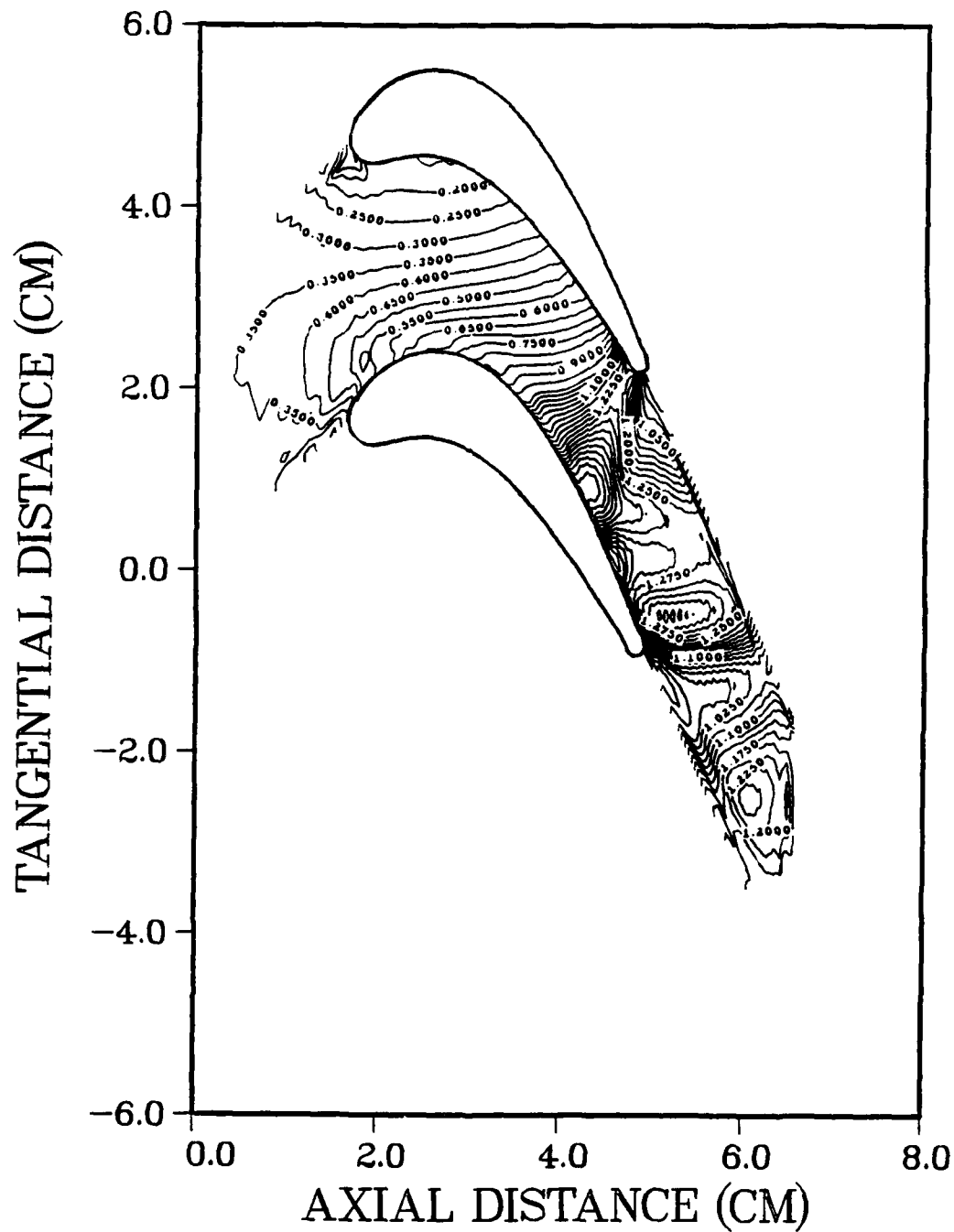
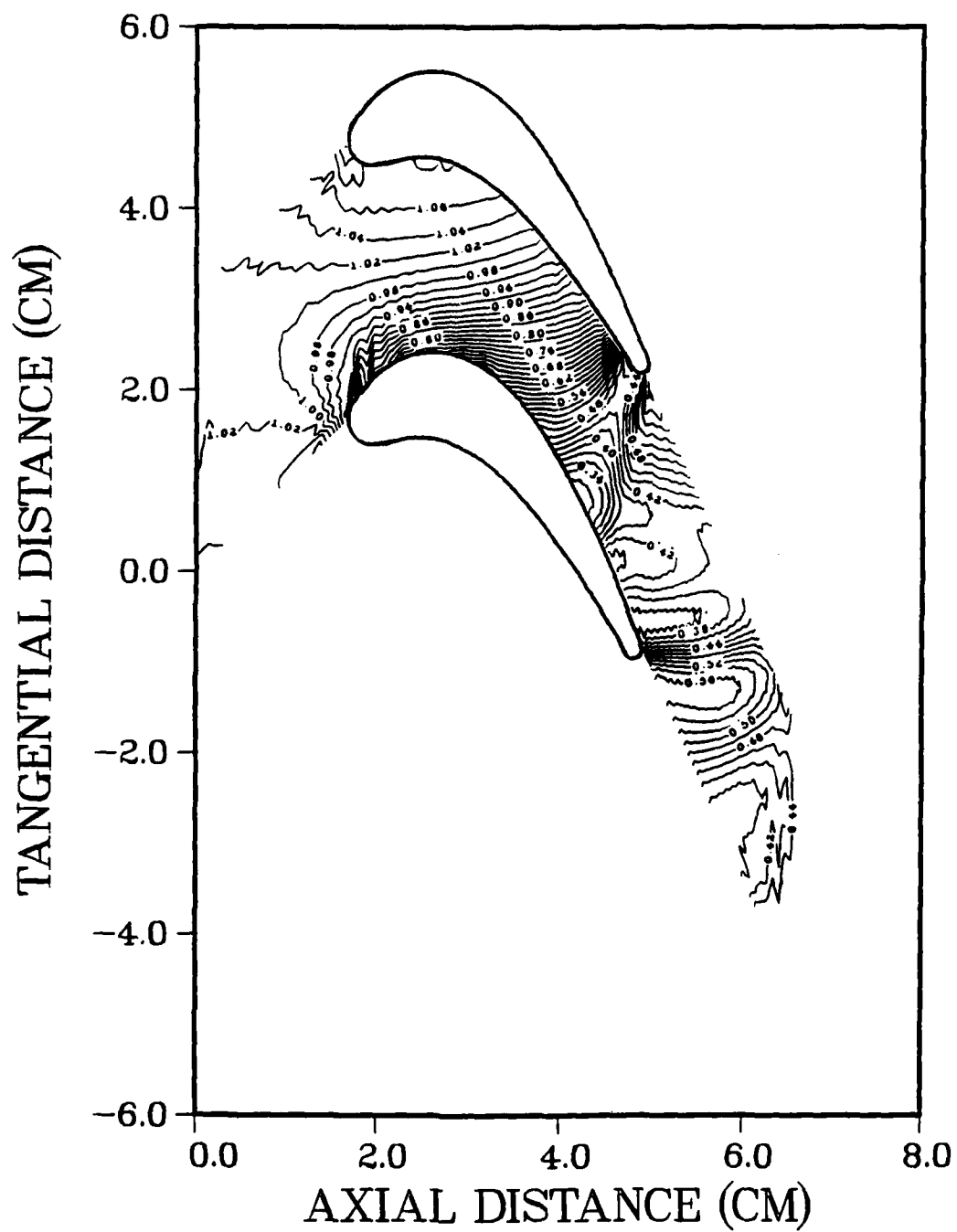Figure 17.   Mach Contours for Case Three

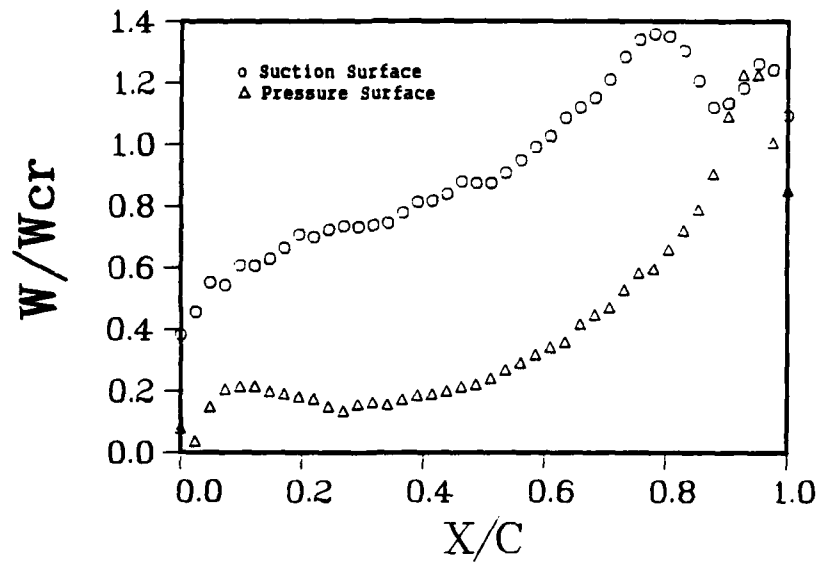Figure 18. Static Pressure Contours (p/p_2) for Case Three

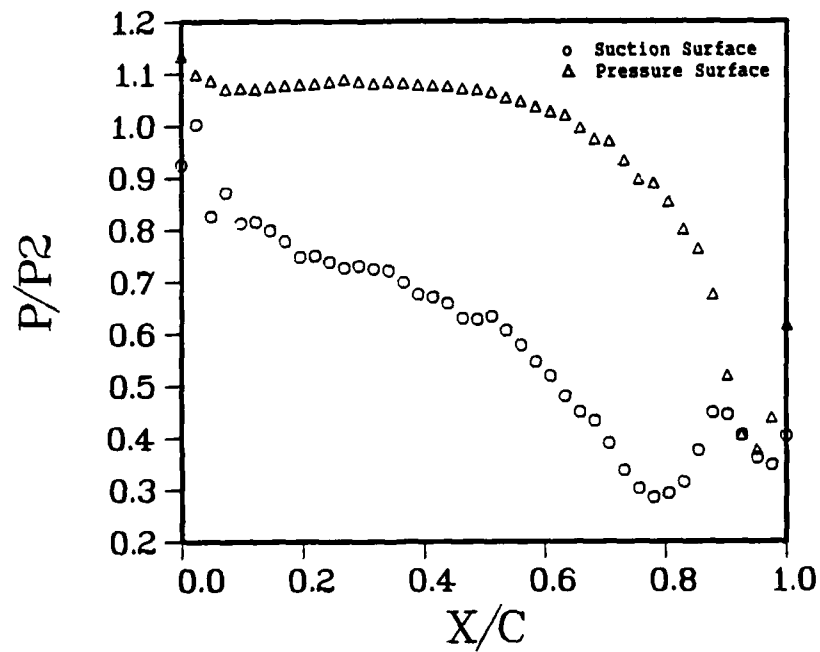**Figure 19.** Blade Loading Diagram for Case Three

Figure 20. Surface Pressures (p/p_2) for Case Three

reattach when the shock impinges farther upstream, as shown in Figure 1. For a typical turbine rotor, the flow separates from the suction surface just prior to reaching the trailing edge. Therefore as the shock impingement point moves closer to the trailing edge the possibility of separation increases. Figure 21 shows the velocity vectors for case three.

Conclusions

A two-dimensional, time marching Euler code has been developed to obtain steady state solutions for flows through transonic turbine cascades. The simple wave theory applied at the radiative boundaries allows any streamwise travelling disturbance to propagate out of the domain without reflection. The method of applying the periodic boundary conditions appears to correctly model the conditions existing in an infinite cascade. The code predicts the formation of two oblique shocks at the blade trailing edges, typical of those experimentally observed in transonic turbine blades. The solutions obtained using the BLD2BLD code compare favorably with the experimental data within certain limits. These limits become evident by comparing computed two-dimensional data, based on an inviscid analysis, with three-dimensional experimental data strongly influenced by viscous effects.

The data processing rate is 2.6×10^{-5} seconds per grid point per time step for the CRAY-XMP computer. The solution

55
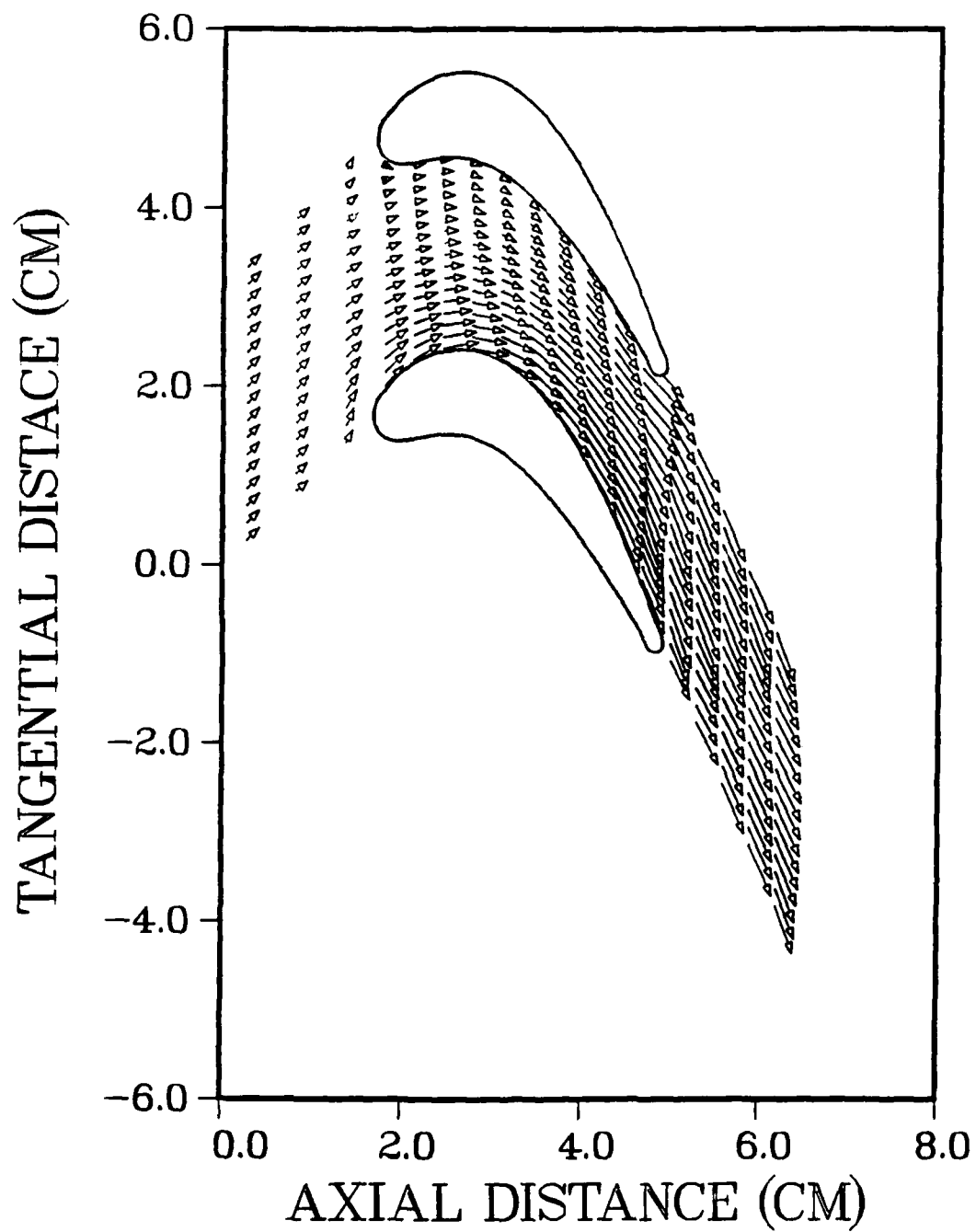
Figure 21. Velocity Vectors for Case Three

56

is monitored until consecutive calculations show less than a
0.02 % change in the dependent variables. The solution is
then considered to be the asymptotic steady state solution.
A typical calculation begun with the cascade tunnel start
initial conditions requires approximately 8000 time steps to
achieve steady state convergence. This translates to 8.69
minutes of CRAY-XMP CPU time for the 76 X 33 grid used for
the NASA turbine case.

V. Recommendations

The areas suggested for further study can be divided into two categories, those related to improving the current ability of the code to obtain steady state blade-to-blade solutions and those related to extending the capabilities to handle unsteady flows and viscous phenomena.

Three specific recommendations apply to the first category. They are

1. Investigate the application of two-dimensional characteristic theory at the periodic boundaries. This should allow the removal of disturbances propagating in the tangential direction with minimal application of explicit numerical damping. A reduction in the damping may allow better shock wave definition and also allow capturing of the reflected shock from the suction surface.

2. Remove the one-dimensional flow assumption at the inlet and exit boundaries. Characteristic theory would still be applied, but in a more general fashion.

3. The effect of grid refinement at the blade leading and trailing edges was not thoroughly investigated during this effort. Grid refinement, especially at the leading edge, should allow better resolution of the flow field near the stagnation points.

The recommendations relating to the second category will require much more effort than those in the first. Two specific areas are suggested for implementation:

1. Viscous effects need to be accounted for. Low aspect ratio turbines are strongly influenced by viscous phenomena and this needs to be accounted for in order to obtain accurate efficiencies.

2. Extend the code to solve the unsteady vane-blade interaction problem. This is the most extensive effort suggested for implementation. Vane-blade interaction is currently receiving much attention in the design community and a code that gives acceptable results has yet to be developed.

BIBLIOGRAPHY

1. Amdahl, Lt David J. Flight Dynamics Laboratory.
   Fortran computer code ORTHGNL. Personal communication.
   HQ AFWAL, Wright-Patterson AFB OH, July 1988.

2. Ames Research Staff. Equations, Tables, and Charts for
   Compressible Flow. NACA Report 1135. Moffett Field
   California, 1953.

3. Anderson, Dale A., John C. Tannehill, and Richard H.
   Pletcher. Computational Fluid Mechanics and Heat
   Transfer. Series in Computational Methods in Mechanics
   and Thermal Sciences. New York: Hemisphere Publishing
   Corporation, 1984.

4. Cohen, H., G. F. C. Rogers, and H. I. H. Saravanamutto.
   Gas Turbine Theory (Third Edition). New York: Longman
   Scientific and Technical, John Wiley and Sons, 1987.

5. Concepts ETI. 1987 Turbomachinery Calendar. Concepts
   ETI, Inc., Norwich Vermont, 1986.

6. Denton, J. D. "An Improved Time Marching Method for
   Turbomachinery Flow Calculation," ASME Paper No.
   82-GT-239, Journal of Engineering for Power, Vol. 105,
   July 1983.

7. Emanuel, George. Gasdynamics: Theory and Applications.
   AIAA Education Series. New York: American Institute
   of Aeronautics and Astronautics, 1986.

8. Erdos, John I. and Edgar Alzner. Computation of Unsteady Transonic Flows Through Rotating and Stationary Cascades, Volume 1. NASA Contractor Report 2900. Contract NAS3-16807. Westbury NY: Advanced Technology Laboratories, December 1977.

9. Gray, Robert. Air Force Aero-Propulsion Laboratory. Private communications. HQ AFWAL, Wright-Patterson AFB Ohio, April through November 1988.

10. Kreyszig, Erwin. Advanced Engineering Mathematics (Fifth Edition). New York: John Wiley & Sons, 1983.

11. MacCormack, Robert W. "Numerical Solution of the Interaction of a Shock Wave with a Laminar Boundary Layer," Lecture Notes in Physics, Volume 8, edited by Maurice Holt. New York: 1971.

12. Mattingly, Jack D., William H. Heiser, and Daniel H. Daley. Aircraft Engine Design. AIAA Education Series. New York: American Institute of Aeronautics and Astronautics, 1987.

13. Oates, Gordon C. Aerothermodynamics of Gas Turbine and Rocket Propulsion. AIAA Education Series. New York: American Institute of Aeronautics and Astronautics, 1984.

14. Press, William H. and others. Numerical Recipes: The Art of Scientific Computing. New York: Cambridge University Pres, 1986.

15. Roache, Patrick J. Computational Fluid Dynamics. Albuquerque: Hermosa Publishers, 1972.

16. Scott, J. N. and W. L. Hankey, Jr. "Boundary
    Conditions for Navier-Stokes Solutions of Unsteady
    Flow in a Compressor Rotor," Three Dimensional Flow
    Phenomena in Fluid Machinery. 141-151. New York:
    Fluid Engineering Division of the ASME, November 1985.

17. Shang, J. S. "Numerical Simulation of Wing-Fuselage
    Aerodynamic Interaction," AIAA Journal, Volume 22,
    Number 10: 1345-1353 (October 1984).

18. Shang, J. S. "Numerical Simulation of Wing-Fuselage
    Interference," AIAA 19th Aerospace Sciences Meeting.
    AIAA-81-0048. (January 1981).

19. Shang, J. S. FORTRAN computer code JSTEST. Private
    communication. HQ AFWAL, Wright-Patterson AFB OH,
    4 April 1988.

20. Stabe, Roy G., Warren J. Whitney, and Thomas P.
    Moffitt. Performance of a High-Work Low Aspect Ratio
    Turbine Tested with a Realistic Inlet Radial
    Temperature Profile. NASA Technical Memorandum 83655.
    Cleveland Ohio: Lewis Research Center, June 1984.

VITA

Captain Mark A. Driver was born ████████████████████
█████████████████ He graduated from Marbury High School
in 1979 and attended Auburn University, receiving the degree
of Bachelor of Aerospace Engineering in March 1984. Upon
graduation, he received a commission in the USAF through the
ROTC program. He was then assigned to the Headquarters
Ballistic Missile Office at Norton AFB, California. While
there he participated in the flight testing of various
preprototype countermeasure systems for the Minuteman III
and Peacekeeper weapon systems. He entered the School of
Engineering, Air Force Institute of Technology, in June
1987.

AD A202706

REPORT DOCUMENTATION PAGE

Form Approved
OMB No. 0704-0188

1a. REPORT SECURITY CLASSIFICATION UNCLASSIFIED	1b. RESTRICTIVE MARKINGS
2a. SECURITY CLASSIFICATION AUTHORITY	3. DISTRIBUTION/AVAILABILITY OF REPORT Approved for public release; distribution unlimited.
2b. DECLASSIFICATION/DOWNGRADING SCHEDULE	

4. PERFORMING ORGANIZATION REPORT NUMBER(S) AFIT/GAE/AA/88D-10	5. MONITORING ORGANIZATION REPORT NUMBER(S)

6a. NAME OF PERFORMING ORGANIZATION School of Engineering	6b. OFFICE SYMBOL (If applicable) AFIT/ENY	7a. NAME OF MONITORING ORGANIZATION

6c. ADDRESS (City, State, and ZIP Code) Air Force Institute of Technology (AU) Wright-Patterson AFB, Ohio 45433-6583	7b. ADDRESS (City, State, and ZIP Code)

8a. NAME OF FUNDING/SPONSORING ORGANIZATION AF Wright Aeronautical Lab	8b. OFFICE SYMBOL (If applicable) POTC	9. PROCUREMENT INSTRUMENT IDENTIFICATION NUMBER

8c. ADDRESS (City, State, and ZIP Code)

Wright-Patterson AFB, Ohio 45433-6583

10. SOURCE OF FUNDING NUMBERS

PROGRAM ELEMENT NO.	PROJECT NO.	TASK NO.	WORK UNIT ACCESSION NO.

11. TITLE (Include Security Classification)
DEVELOPMENT OF A SHOCK CAPTURING CODE FOR USE AS A TOOL IN DESIGNING HIGH-WORK LOW ASPECT RATIO TURBINES

12. PERSONAL AUTHOR(S)
Mark A. Driver, Capt, USAF

13a. TYPE OF REPORT MS Thesis	13b. TIME COVERED FROM _____ TO _____	14. DATE OF REPORT (Year, Month, Day) 1988 December	15. PAGE COUNT 75

16. SUPPLEMENTARY NOTATION

17. COSATI CODES

FIELD	GROUP	SUB-GROUP
21	05	

18. SUBJECT TERMS (Continue on reverse if necessary and identify by block number)
Engines, Gas Turbines, Turbine Blades, Numerical Analysis
Inviscid Flow, Shock Waves

19. ABSTRACT (Continue on reverse if necessary and identify by block number)

Thesis Advisor: Dr. Ahmed A. M. Halim
                 Associate Professor of Aerospace Engineering

12 Jan 1989

20. DISTRIBUTION/AVAILABILITY OF ABSTRACT ☒ UNCLASSIFIED/UNLIMITED ☐ SAME AS RPT. ☐ DTIC USERS	21. ABSTRACT SECURITY CLASSIFICATION UNCLASSIFIED
22a. NAME OF RESPONSIBLE INDIVIDUAL Ahmed Halim, Assoc. Prof. of Aerospace Eng.	22b. TELEPHONE (Include Area Code) 513-255-3517	22c. OFFICE SYMBOL AFIT/ENY

DD Form 1473, JUN 86   Previous editions are obsolete.   SECURITY CLASSIFICATION OF THIS PAGE

A numerical algorithm is developed with the capability
of capturing shocks in the internal blade passages of a
modern gas turbine. The algorithm uses MacCormack's
explicit finite difference scheme to solve the two-
dimensional form of the Euler equations. Inlet and exit
boundary conditions are developed that allow disturbances to
propagate out of the computational domain without
reflection. Periodic boundary conditions are applied such
that an infinite cascade is modeled.

The computed steady state solution is compared with
experimental data for a high-work low aspect ratio turbine.
The ability to obtain a reasonably accurate blade loading
diagram within a practical execution time is demonstrated.
Two oblique shocks, typical of those formed at the trailing
edge of a transonic rotor blade, are captured. These shocks
are smeared over several grid points, as expected with a
shock capturing scheme, but their influence on the blade
loading diagram is evident.